2019-07-22

Towards the automatic control of laser ablation for surgical applications

Karim A. Tarabein

Towards the automatic control of laser ablation for surgical applications

by

Karim Tarabein

A Thesis

Submitted to the Faculty

of the

WORCESTER POLYTECHNIC INSTITUTE

In partial fulfillment of the requirements for the

Degree of Master of Science

in

Biomedical Engineering

by

August 2019

APPROVED:

_____

Professor Loris Fichera, Major Thesis Advisor

_____

Professor Glenn Gaudette, Thesis Committee Chair

_____

Professor Matthew C. Flegal, Thesis Committee Member

Abstract

The goal of this thesis is to propose and investigate a method of predicting depth of a laser dissection pulse in soft tissue without acquiring material properties of the tissue target or measuring the laser output. The method proposed is similar to what is used by laser surgical operators today, but uses regression learning to perform on-the fly predictions in place of a skilled laser surgeon. Power of the laser and the ablation depth were recorded for 57 samples and fed into the regression algorithm. Data exclusion was performed using Temperature before laser action as criteria. A linear and logarithmic model was explored using random points from the data post-exclusion, validation RMSE ranged from 135-200 μm. A linear and logarithmic model was explored using data points below a moving power threshold and validated with data points above said threshold, validation RMSE ranged from 108-170 μm. The t.test performed showed there was not a significant difference between the linear and the logarithmic models' goodness of fit metrics, but it did show there was a significant difference between the model building methods (randomly selected data points, moving power threshold). The method of building a model using lower power levels to predict larger power levels had better goodness of fit metrics than the method of selecting data points at random. In the future, this method could be used to help approximate the laser settings for surgery on a procedural basis, and allow for surgeons to perform at a higher skill level with less training.

Acknowledgements

I would like to acknowledge and express gratitude towards Dr. Bob Rudko with Laser Engineering co. for modifying our laser system and for providing extensive assistance in procuring equipment such as laser waveguides for the purpose of this thesis.

I would like to express my gratitude towards my thesis advisor, Dr. Loris Fichera, for giving me the opportunity to work on this research project. I would also like to express gratitude towards my committee members (Dr. Glenn Gaudette, Dr. Cosme Furlong, Dr. Matthew Flegal) for their outstanding help and guidance during the entirety of this thesis project.

I would like to thank WPI's Biomedical Engineering Graduate department for allowing me to pursue this thesis topic, and for allowing me to cultivate and improve upon my skills in a challenging and professional environment.

Lastly, I would like to thank my Jeddo, Jamal Al Fakir. His accomplishments as an engineer, business man, UN Officer, and world traveler have inspired me to this day.

"Three things to remember: 1) Think globally but act locally, 2) It is your duty to plant love wherever you go, and 3) No matter how high the hill or obstacle, determination is the vehicle used to overcome it." -Jeddo Jamal-

Contents

List of Figures

List of Tables

Chapter 1

Introduction

1.1 Motivation

Lasers are routinely used in clinical surgery as cutting instruments. The benefits of laser surgery are manifold: lasers can simultaneously cut, sterilize, and cauterize vessels, thus providing excellent hemostasis [1, 2, 9]. In microsurgery (also referred to as microscopic surgery), lasers are particularly attractive because they can be focused in tiny diameters, and their wavelength can be chosen in such a way to limit penetration into tissue [2, 9]. In spite of these benefits, lasers remain challenging when compared to other tools in a surgeons arsenal. Surgical laser systems present many operational parameters (power, focusing level, pulse duration, distance from fiber tip to tissue target, etc.) where a beam can either emitted as a free beam or be passed through a fiber or waveguide [1, 2, 9]. Control of these many parameters is not intuitive to the designated operator; surgeons are classically trained to cut through tissue using scalpels, scissors, and blunt instruments using a variety of dissection techniques, and to use their delicate sense of touch as feedback to guide their actions. In minimally invasive procedures, where surgical lasers see operational

use as a replacement for a scalpel, the issue of control is compounded by the difficulty of deployment and operation in small spaces within the human body. As such, there is a steep learning curve associated with performing laser surgical dissection and resection procedures, especially in minimally invasive applications.

1.2 Scope of the thesis

In this thesis, we describe the concept of a new technology capable of automatically performing surgical laser cutting based on high-level surgeon commands (for instance, specifying the specific depth of cut desired). Our hope is that this technology will make using surgical lasers more intuitive to use and contribute to expanding the pool of laser surgeons. To realize this vision, we propose to combine robotic technology with new methods to model and control laser-tissue interactions: we envision a system where surgeon commands are interpreted by a computer program and used to synthesize a surgical action plan that is then executed by a robot.

As a first step in this investigation, this thesis focuses on the problem of finding the laser parameters required to obtain a prescribed incision depth "on the fly," ie. while in the operating room. We propose to develop models based on statistical learning algorithms that describe the relation between the application of laser parameters and the cutting depth. These models will enable us to investigate model-based control schemes for surgical laser cutting processes.

1.3 Contributions

The contributions for these thesis are:

- Developed Bench test for these experiments and future experiments

- Developed and validated Data acquisition method
- Sample tests and preparation
- Design of Experiment
- Preliminary data acquisition to validate early claims

In section 4.1, found under materials and methods, I go into more detail on the thought process for the formulation of each of these contributions. More details on my personal contributions can be found in Appendix B and C.

Chapter 2

Fundamentals of Laser-Tissue Interactions

Medical applications of lasers have been explored ever since the creation of the first laser source back in 1960 [2, 7]. One of the early challenges, still subject of scientific inquiry at present days, was to model and control the physical interactions that occur between laser light and biological tissue in order to achieve a desired treatment [6, 7]. This chapter provides an introduction to the physics of laser-tissue interactions. Special emphasis will be given to laser dissection via thermal ablation, which is the main focus of the study reported in this thesis.

2.1 Laser Light

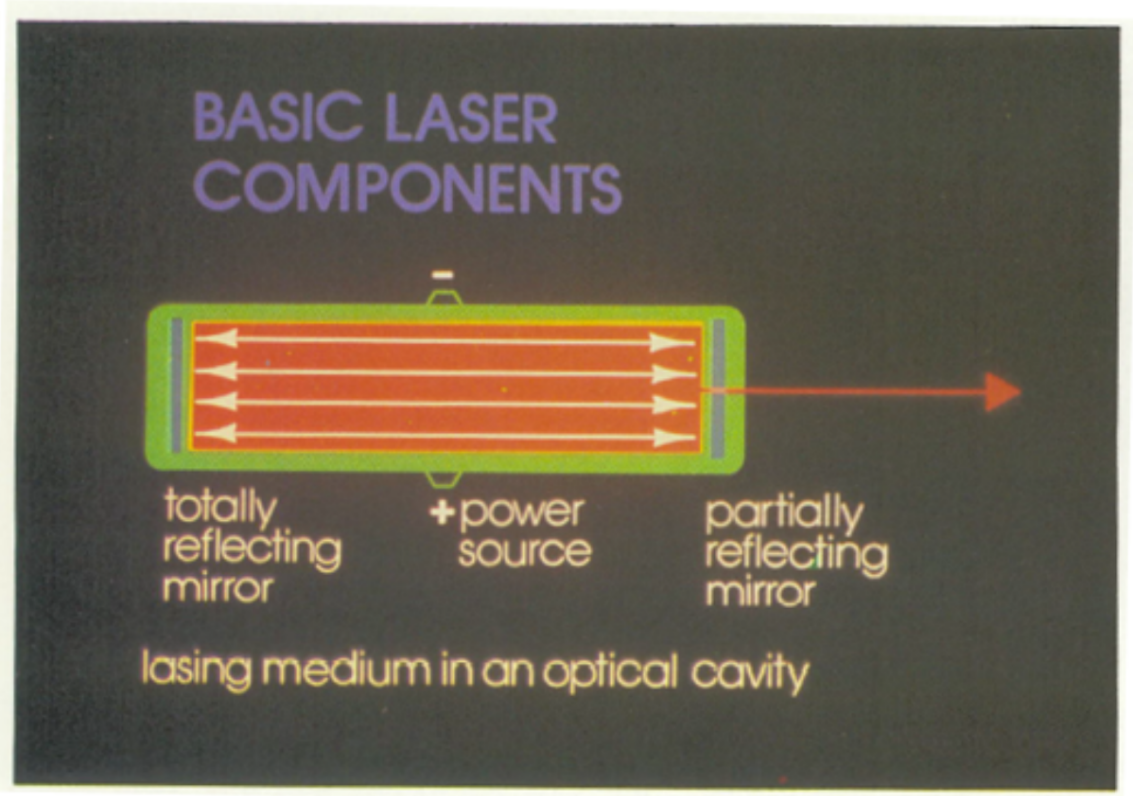

Figure 2.1: Diagram showing basic laser components for the production of laser light. Reproduced from Atlas of CO2 Lasers [1].

The term "Laser," an acronym for *Light Amplification by Stimulated Emission of Radiation*, refers to a class of devices that produce an intense beam of highly collimated, monochromatic light [1, 2]. This is accomplished via stimulation of a medium using light that leads to an emission of a specific wavelength of radiation from said medium. This process is also referred to as "stimulated emission", illustrated in Fig. 2.1. The emitted wavelength is dependent on both the medium, the stimulation wavelength, and phase of the stimulation.

2.1.1 Laser Beam Characterization

Free beam propagation refers to any point in time when a laser beam travels through open space, including the times when the laser beam leaves a fiber or waveguide. The distribution of the laser intensity profile is largely dependant on the boundary conditions of the cavity in the laser device and the mirrors used to confine light through it. Surgical laser systems are usually constructed in a way where the intensity of the beam can be characterized in a Gaussian-shaped function whose peak lies on the optical axis z and are described through a combination of a Gaussian function with a generalized Laguerre Polynomial of an order l and index p, ie L_p^l. Assuming a cylindrical reference frame (r, φ, z), with z denoting the beam axis, r and φ being polar coordinates of a plane transverse to z, the intensity profile is defined as [2]:

$$I_{pl}(r, \varphi, z) = I_0 \rho^l [L_p^l(\rho)]^2 \cos^2(l\varphi) exp(-\rho) \tag{2.1}$$

where I_0 is maximum intensity, and $\rho = \frac{2r^2}{w^2(z)}$. $w(z)$ is referred to as the spot size of the beam, or the radius at which the intensity of the beam is equal to I_0/e^2 [2]. The indices, l and p are integers that determine the shape of the intensity profile shown in Fig. 2.2.

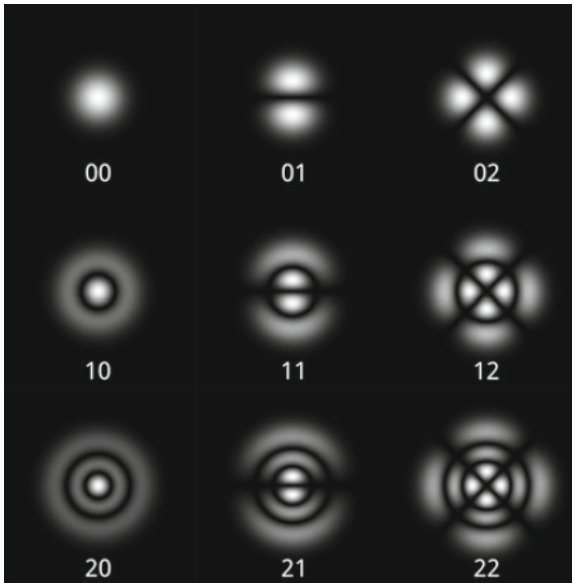

Figure 2.2: Transverse modes of Gaussian Beams for different values of l and p. Higher values of intensity are represented with brighter shades of gray. Reproduced from Fichera [2]

The l and p integers for most surgical laser systems are 0 and 0, as the other shapes represented in Fig. 2.2 do not have practical uses in the field of laser surgery yet. These beams are referred to as Gaussian beams, and their intensity distribution can be described as [6]:

$$I(r,z,t) = I_0 exp(-\frac{2r^2}{w_0^2} - \mu_a z) exp(\frac{-8t^2}{\tau^2}) \tag{2.2}$$

Where w_0 is the laser beam waist, t is the total exposure time, and τ is the pulse duration. The optical absorption coefficient, μ_a, is negligible when traveling through vacuum or non-absorbing material such as air in an operating room. Laser beam waist is defined as the minimum radius of the laser beam when focusing reaches its maximum as seen in Fig. 2.3. Gaussian-shaped beams present a relatively

low divergence and maintain a Gaussian shape along each cross-section along the propagation axis, z [2].

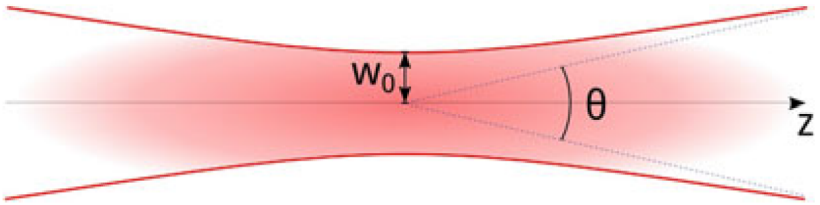

Figure 2.3: Propagation of a laser beam along optical axis z, divergence angle θ, the spot size where the beam is most focused w_0. Reproduced from Fichera [2]

One can calculate the power distribution of the laser along the target's surface by multiplying the intensity profile, $I(r, z, t)$, with the matching optical absorption coefficient, μ_a, for the wavelength used.

$$S(r, z, t) = \mu_a I(r, z, t) \tag{2.3}$$

The variable $S(r, z, t)$ becomes important when looking at heat generation through tissue using a heat source, in this case a laser beam. This is in anticipation of later sections when discussing the laser tissue interactions and the physics involved.

2.1.2 Beam propagation through a fiber

Often times, surgery is conducted by delivering the laser light through flexible delivery system such as a laser fiber [1, 9]. In laser fiber propagation the beam travels through a flexible, solid medium. The medium refracts the beam, changing direction or angle of incidence within the walls of the fiber. As shown in Fig. 2.4, the angle of incidence (shown in the figure as the "Angle of Light") usually decreases when

travelling from air into another medium.

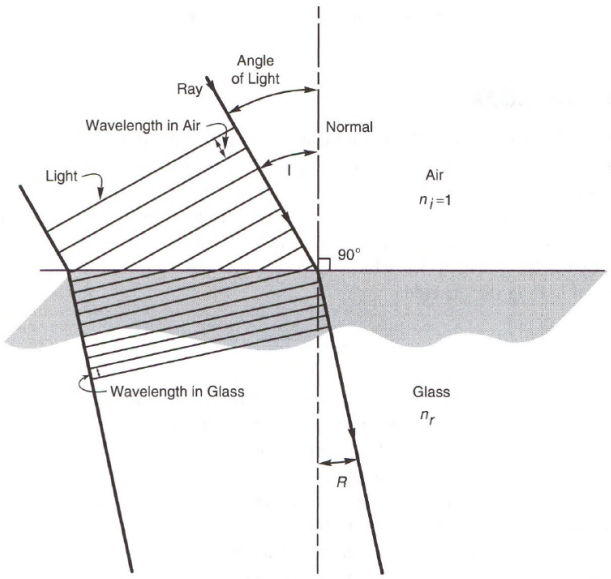

Figure 2.4: Refraction of light entering glass. Reproduced from Hecht [3]

The main advantage of propagating a laser beam through a fiber is the ability to direct the laser beam along the fiber with minimal power loss. This is possible due to a particular property of light when it collides with a surface: total reflection. When a beam of light collides with a surface, some of the energy is refracted. If the angle between the laser beam and the surface it collided with is small enough, most of the energy in the refracted beam is reflected. In the particular case of the laser fiber, or the laser beam traveling through its core reflects internally when it comes in contact with the fiber cladding, and which coalesces into multiple total reflections inside the fiber until the beam exits [3]. In the study of fiber optics, this is referred to as total internal reflection [3]. This allows for the fiber to guide the laser beam along it's path via numerous low angle reflections, where it refracts again upon exiting the fiber tip and enters a new medium.

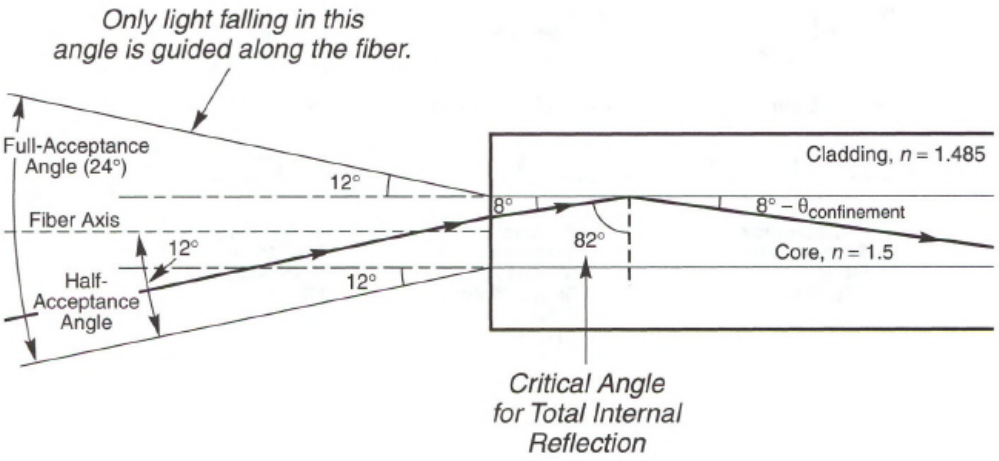

Figure 2.5: Light guiding in a large-core step-index fiber. The confinement angle measures the angle between guided light rays and the fiber axis; the acceptance angle is measured in air. Reproduced from Hecht. [3].

The angle of confinement (the minimum angle where total reflection occurs) is completely dependant on the refractive indices, n_{core}, of the medium the beam is traveling through and the medium the beam collides with, n_{clad}. In the case of laser fibers, both the critical angle and angle of confinement depend on the n of the internal medium and the cladding of the fiber [3].

$$\theta_{confinement} = \cos^{-1} \frac{n_{clad}}{n_{core}} \tag{2.4}$$

As long as the angle between the cladding and the beam is less than the angle of confinement, total reflection will occur and guide the light along the fiber via total internal reflection along the core. It is important to note that while the phenomena is referred to as total internal reflection, there is still some small amount of energy loss that occurs as the laser travels along the path of the fiber [3].

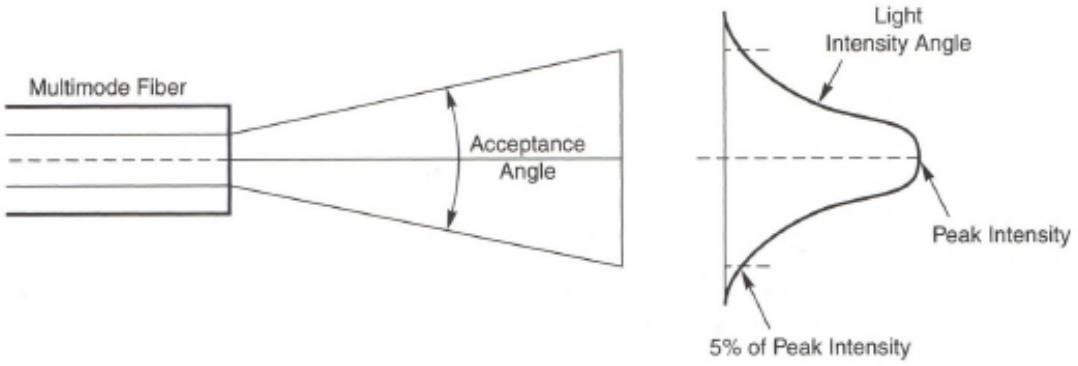

Figure 2.6: Intensity of light emerging from a multimode fiber falls to about 5 percent of peak value at the edge of its acceptance angle. Reproduced from Hecht [3]

As the beam leaves the fiber and propagates through the air, the beam diverges out in a cone shape as seen in Fig. 2.6. The standard measure of the acceptance angle and divergence angle is referred to as Numerical Aperture (NA).

$$NA = \sqrt{(n_0^2 - n_1^2)} = \sin\theta \tag{2.5}$$

The spot size, w_z, of the laser relates to the angle of the beam exiting the fiber and can be roughly calculated as

$$w_z = \pi r^2 = \pi(z \sin(\theta_{divergence}))^2 \tag{2.6}$$

Where z is the distance from the fiber tip to the target, and $\theta_{divergence}$ is the divergence angle. Spot size is an important metric to consider in laser surgery and helps determine the two dimensional power density of the laser on the tissue surface. Eqn. 2.6 is the same equation for the area of the circular base of a cone using a radius calculated using $\theta_{divergence}$ and distance from the target z. Simply by moving the

fiber tip away from the target, the surgeon can increase the spot size and decrease the power density of the laser, which generally leads to a lower ablation depth [1]. Two dimensional power density plays a critical role in determining which laser-tissue interaction occurs and is a factor in laser ablation depth. The importance of the two dimensional power density is further described in section 2.2 and section 3.1.

2.1.3 Beam propagation through a Waveguide

Beam propagation through a hollow-core waveguide is very similar to beam propagation through a laser fiber, with the key difference that the beam does not transmit through a new medium before being directed by the waveguide and instead travels through the hollow-core [4]. Similarly to a fiber, waveguides direct beams of light through total internal reflection, in this case through a hollow cavity [4]. Waveguides still allow for propagation of most of the beam via total internal reflection, as long as the angle between the light beam and the cladding is less than the angle of confinement. As noted before, presence of refraction as the beam enters a solid medium fiber changes the angle of incidence of the beam upon entry. Because there is no transition between media upon the beam entering the waveguide, the angle between the fiber axis and the beam remains unchanged before total internal reflection, illustrated in Fig. 2.7.

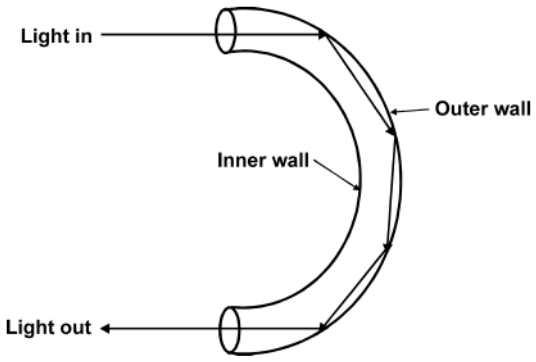

Figure 2.7: Geometry of bent hollow-core waveguide demonstrating the path of a beam through total internal reflection. Reproduced from Harrington. [4]

Similarly to laser fibers, the beam exits the waveguide in a cone shape as seen in Fig. 2.8. The spot size of the lase, w_z, and the two dimensional power density on the tissue target surface are both dependent on the distance the beam has to travel from the end of the waveguide to the tissue target. In waveguides, the divergence angle can be calculated as

$$\theta_{divergence} = \frac{u_{1m}\lambda}{2\pi a} \tag{2.7}$$

Where $\theta_{divergence}$ is the divergence angle, λ is the wavelength of the laser, a is the radius of the hollow core, and u_{1m} is a coefficient that depends on the order number of the laser mode [5]. The relationship shown in the equation describes how the bore radius and the wavelength of the laser affect the divergence angle of the beam, and subsequently the two dimensional power density.

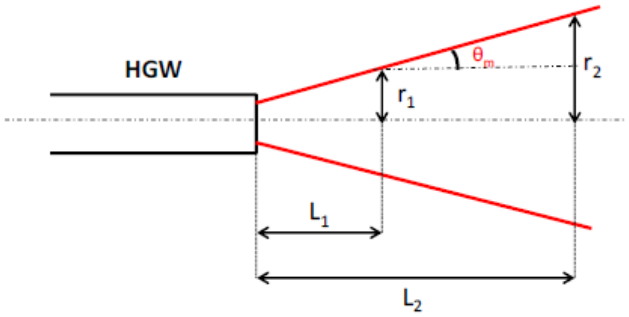

Figure 2.8: Geometry of the beam exiting a hollow core waveguide, L_1 and L_2 are measurements along the beam axis at different points, r_1 and r_2 are measurements of the radius of the beam cone along different points. Reproduced from Patimisco. [5]

Alternatively, it is more practical to calculate the output divergence angle using the change in radius of the beam cone along the cone's axis [5]

$$\theta_{divergence} \approx \tan \frac{r_2 - r_1}{L_2 - L1} \tag{2.8}$$

While this equation does not give the exact divergence angle, it is more feasible to calculate if one is missing information for the laser.

2.2 Classification of Laser-Tissue Interactions

After having reviewed the fundamental concepts of laser light generation and propagation, we are now ready to discuss the physical interactions that occur between laser light and biological tissue.

Free beams interact with matter differently based on the angle of incidence, the angle between the beam and the normal to the surface of the matter it collides with, and the absorption coefficient of the matter, which describes how much of the light

transmitting through a medium is absorbed and converted into heat. If the beam is perfectly perpendicular with the matter and the matter does not absorb any energy from the light beam, as is rarely the case, the beam is then transmitted through the matter. If the beam is not perpendicular to the surface, some of the beam reflects off the surface and the remainder refracts through the surface. Refraction occurs when light changes the medium it is travelling through, resulting in the beam changing direction upon passing through the new medium. Attenuation, a decrease in the beams power, occurs when some of the energy of the beam is absorbed during refraction or transmission. These phenomena are not isolated, more often than not there will be some combination of reflection, attenuation, refraction, and transmission depending on the light and material properties.

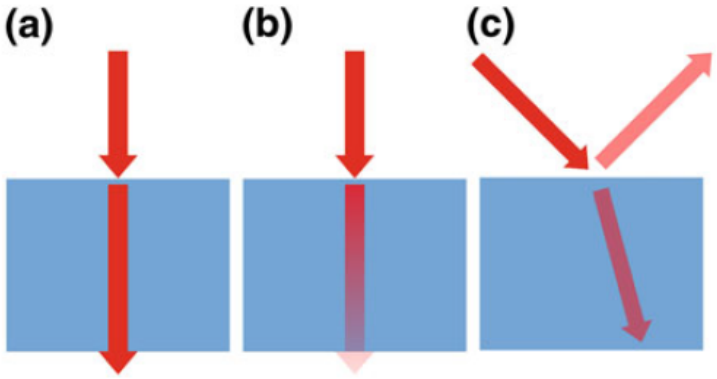

Figure 2.9: Basic interactions of laser light with matter. Here, the beam is directed onto the surface of a block. Depending on the properties of the beam and the material, three different interaction mechanisms may occur: (a) Transmission (b) Attenuation (c) Reflection and Refraction. Reproduced from Fichera. [2]

In general, when a laser beam is applied to tissue, a variety of different physical phenomena can occur. A high-level classification of these mechanisms can be made

by considering (1) the power density of the laser beam and (2) the total duration of laser exposure, as shown in Fig. 2.10

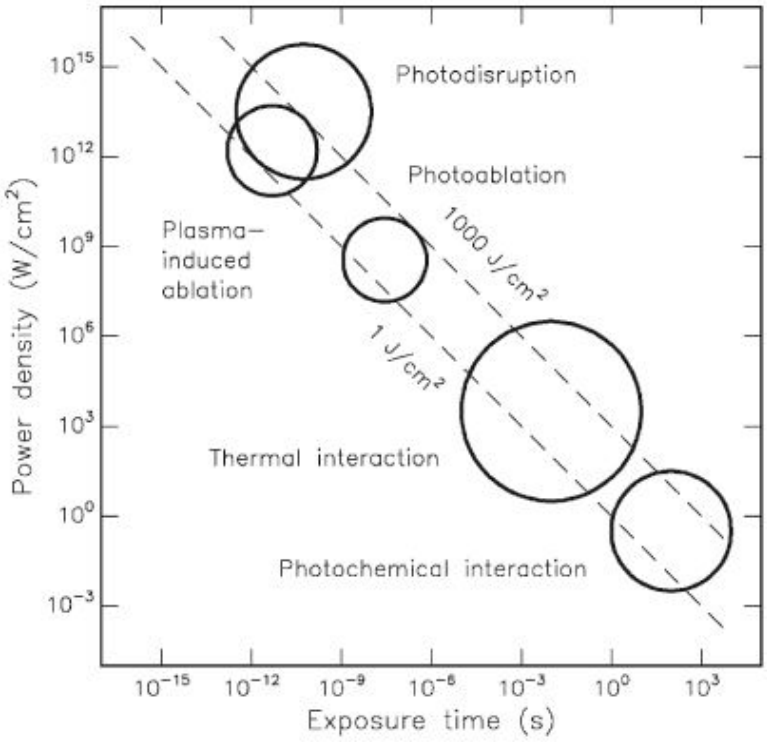

Figure 2.10: Taxonomy of laser-tissue interactions. Reproduced from Niemz.[6]

These interaction mechanisms have one thing in common: they all reside in a band where energy density is between 1 and 1000 J/cm2 as seen in Fig. 2.10. Another interesting aspect of this classification is that it does not make any assumptions of the characteristics of the tissue! This does not mean that tissue properties (e.g. absorption) are not important - they are! - they will be addressed more in section 2.2. Most laser surgical systems, such as the one being used for this thesis, fall under the classification of "Thermal Interactions", where the power density is between 10-10^6 W/cm^2 and exposure time varies between a few milliseconds and up to several seconds.

As we should see in the following, modeling the Thermal Interactions in tissue can be quite difficult for a multitude of reasons, the primary cause being the non-homogeneity of structural and thermal properties of tissue and the differences in the optical absorption of tissue in location, time, and patient [1, 2, 7, 10, 11, 12].

2.3 Thermal Interactions

Thermal interactions are characterized by the fact that vaporization via tissue temperature increase contributes the most towards thermal ablation. When tissue temperature reaches a certain threshold, vaporization occurs in the target which in turn leads to the creation of an ablation crater. This vaporization causes an ejection of tissue material from the target in the form of an ablation plume, the resulting mechanical forces of this eruption is referred to as *Thermal Decomposition* [6]. Despite this, the governing parameter for all laser-tissue thermal interactions is Temperature, with thermal vaporization being the primary mechanism in the creation of ablation craters [6]. In soft tissues, the temperature threshold for vaporization is usually around 100 C, the boiling point of water within cells, upon which vaporization can occur [1].

2.3.1 Thermal Vaporization

Let us entertain that the general idea of a model where when a temperature threshold is reached (100 C), vaporization can occur. How difficult would it be to calculate the variation of temperature in a sample of tissue exposed to a laser beam? In a closed system, change of energy dQ increases linearly. In practical applications of laser-tissue interactions, however, there are losses of heat to take into account. The change of energy dQ (Joules) can be defined as a function of the change of

temperature in Kelvin ΔT, specific heat C $(J/Kelvin)$, and mols of material m.

$$dQ = mC\Delta T \tag{2.9}$$

The mechanisms of thermal transfer within the tissue are based on *heat conduction, heat convection* or *heat radiation*. Depending on the tissue and its perfusivity, heat convection can be ignored for some tissues with low perfusion. Only in longer exposures is the heat loss from blood flow significant [6]. Heat radiation can also be neglected due to the moderate temperatures created in thermal interactions [6]. The conduction of heat is the primary mechanism through which heat is transferred to adjacent tissue and contributes the highest heat loss to the target. Our starting point is the *equation of continuity* which states that the temporal change in heat content per unit volume, $\dot{q}$, is determined by the divergence of the heat flow, jQ [6]:

$$divjQ = -\dot{q} \tag{2.10}$$

Inserting eqn 2.10 into 2.9 leads to:

$$\dot{T} = \frac{1}{mc}\dot{Q} = -\frac{1}{\varrho c} divj_q \tag{2.11}$$

Where $\dot{T}$ is the change in temperature (Kelvin), ϱc is inversely proportional to conductivity of heat κ, and $divj_q$ is the divergence of heat flow. The other important piece is the diffusion equation [6]:

$$jQ = -\kappa \nabla T \tag{2.12}$$

When combined with eqn 2.11, it yields [6]:

$$\dot{T} = \kappa \nabla^2 T \tag{2.13}$$

In the absence of a phase transition or photochemical reaction, the energy absorbed via laser pulse is completely absorbed and converted into temperature [6]. Adding the heat source from the laser, represented by variable S (Joules), transforms the previous equations to non-homogeneous equations [6].

$$\dot{T} = -\frac{1}{\varrho c}(div j_q - S) \tag{2.14}$$

$$\dot{T} = \kappa \nabla^2 T + \frac{1}{\varrho c} S \tag{2.15}$$

Solving for the homogeneous portion of the conduction equation describes the decrease in temperature after laser exposure due to heat diffusion using cylindrical coordinates.

This of course assumes isotropic thermal and optical behavior in the tissue, which is not quite the case for a number of soft tissues operated on in laser surgery [6, 11]. Recall how the equation $S(r, z, t) = \mu_a I(r, z, t)$ shows the relationship between the energy delivered via laser beam, $S(r, z, t)$, is dependent on the optical absorption coefficient μ_a. This would make the energy added via the laser non-homogeneous as tissue targets may have a large variance in μ_a [6, 11].

There are some limitations that should be addressed regarding these equations, as they do not take into account material removal which occurs concurrently with additional energy according to Vogel and they rely on the knowledge of a number of physical coefficients that 1) have high variance in different parts of the tissue target making approximation of these variables using previous tests unreliable, 2) are impractical to estimate in a surgical operating room, 3) even if one extracts the parameters, it remains a difficult task to have the surgeon select the laser parameters

of the procedure based off of desired $S(r, z, t)$ or $I(r, z, t)$ [6, 7, 12].

2.3.2 Modeling the material removal rate

Alfred Vogel proposed a steady state model to describe the material removal and ablation depth for laser tissue interactions that fall under "Thermal Interactions" [7]:

$$depth = \frac{E - E_{th}}{\rho h_{abl}} \tag{2.16}$$

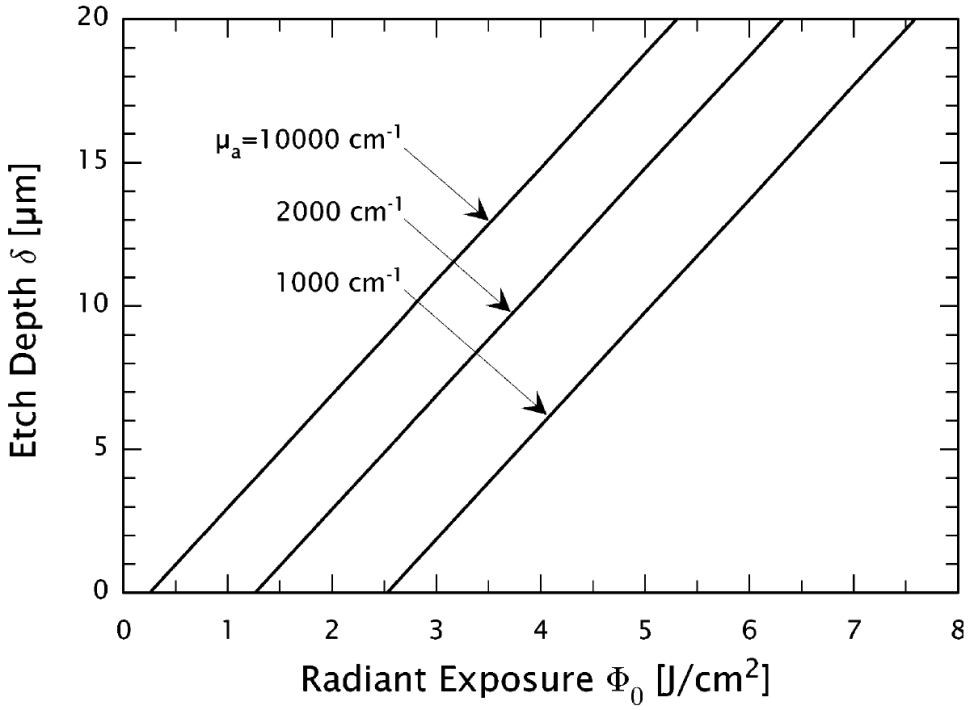

Figure 2.11: Theoretical Steady-State model for different absorption coefficients and constant $h_{abl} = 2580$ J/g. Reproduced from Vogel. [7]

Where E is the energy density J/cm^2 created by the laser beam on the surface of the tissue target, E_{th} is the minimum energy density required to trigger vapor-

ization and is inversely proportional to the optical absorption coefficient μ_a, h_{abl} is the ablation enthalpy J/kg which is related to the optical absorption coefficient of the tissue, and ρ is tissue density kg/cm^3. This steady state model assumes that material removal is time invariant, that a delivery of a threshold radiant exposure is required to initiate material removal, and that material removal is concurrent with the delivery of the energy. The model suggests that once the threshold is met, a linear relationship is observed if density and ablation enthalpy remains the same [7]. As previously mentioned, the optical absorption coefficient of the tissue is highly variable, which implies a more complicated reality than the linear model proposed by Vogel. Every tissue from every donor has different optical absorption coefficients between different times of measurement, during ablation, and different locations on the tissue [11].

Chapter 3

Use of Lasers in Laser Surgery

In the last chapter we saw that laser can add heat to tissue and raise the temperature. Adding heat can be used for a variety of purposes, including tissue regeneration to destructive procedures such as vaporization [12]. Here we review how lasers are used in medicine and we focus particularly on their use in surgery.

Table 3.1: (*) CW = Continuous Wave Mode, SP = Super Pulse Mode, P = Pulser Mode. Tissue effects and recommended laser settings for Lumenis 30C CO_2 laser surgical system, recreated from Lumenis 30C instruction manual [8].

Tissue Effects	**Average Power**	**Spot Size**	**Preferred Mode ***	**Beam Manipulation**
Deep Incision	High	Focuses	CW, SP, P	Slow
Shallow Incision	Low	Focused	SP	Slow
Shallow Incision	High	Focused	CW, SP	Fast
Bulky Vaporization	High	Defocused	CW, P	Slow
Superficial Vaporization	Low	Defocused	CW	Slow
Superficial Vaporization	High	Defocused	CW	Fast
Coagulation	Low	Defocused	CW	Slow
Coagulation	High	Defocused	CW	Fast

Depending on the system and the tool used to direct the laser, the physician can use the same tool to sterilize, cauterize, ablate, dissect, and resect tissue as demonstrated in Table 3.1; its versatility is akin to the scalpel blade and is a powerful tool for surgical operators to use when precision and hemostatic cutting is desired [1, 2, 8, 9]. Surgical Lasers see a wide array of use between different disciplines that treat soft tissues both in open surgery and minimally invasive surgery, including but not limited to: gastroenterology, cardiology, ophthalmology, neurology, and dermatology [1, 2, 9, 10, 13, 14]. Surgical lasers are also a desireable tool for microsurgery: ie surgical procedures in a small area, often done using scopes with magnification [2, 9, 14].

In the medical literature, the use of laser technology is reported for mainly two purposes: tissue *ablation* and tissue *dissection* [1, 9]. Use of these terms may create

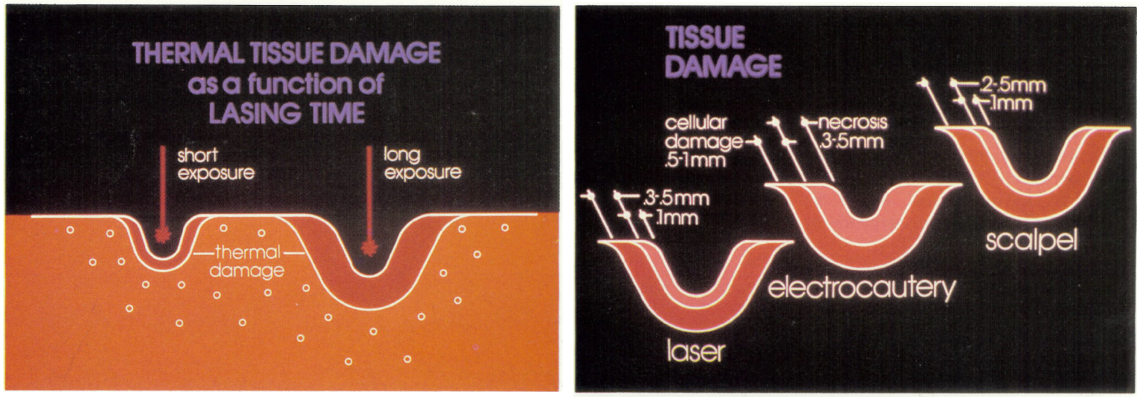

Figure 3.1: Long vs Short exposure effects on tissue. Reproduced from Atlas of CO2 Lasers [1].

some confusion, as the same terms are used in other fields of study with slightly different meaning. In physics, for instance, tissue ablation generally refers to the process of removing material from tissue. For the purpose of this thesis, we consider laser ablation as a procedure whose goal is bulk vaporization of diseased tissue (e.g. a tumor metastasis). Dissection and resection is instead defined as the process of cutting through tissue to excise an entire specimen, typically a benign or malignant tumor. These differences are illustrated in Fig. 3.2.

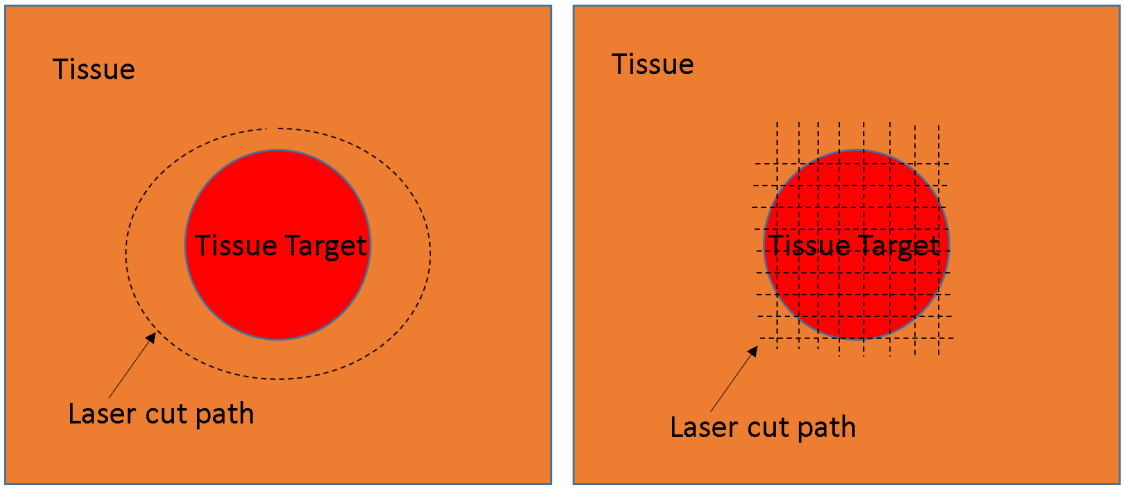

Figure 3.2: Comparison of laser resection (left) and laser ablation (right) in treating diseased tissue, labeled "Tissue Target".

For dissections or resections, thermal damage spread is an undesired affect. Minimal residual tissue damage (such as thermal damage spread) is desired [1, 9]. For ablative procedures, thermal damage spread might be a desired. Higher thermal damage spread might be beneficial as it would ensure any remaining diseased tissue that was not vaporized becomes necrotic [1, 9]. The thesis will focus on the problems associated with creating proper incisions using laser dissection or resection, specifically gauging ablative incision depth. Moving forward, the depth of a laser surgical "incision" made using a single pulse will hereto be referred to as "laser pulse depth" or "ablation depth".

3.1 Surgical Laser Cutting of Soft Tissue

While various wavelengths of lasers are used to target different media more efficiently, CO_2 lasers are used for numerous medical applications across different fields

due to their ability to vaporize anything composed of a significant amount of water molecules (ie. soft tissue cells).

This cellular vaporization also adds security when targeting cancerous tissue by burning any potential cancer cells surrounding the target and killing them. In addition, CO_2 lasers reduce " operative blood loss by improved hemostasis... Blood vessels and lymph vessels up to 0.5 mm diameter are sealed by the laser, which also provides immediate sterilization to the effected site [1]. The CO_2 laser is a popular choice for many soft tissue procedures because unlike other lasers, the pigment of the tissue has little to no effect on the characteristics on the laser cut or ablation [1]. Because of its wide clinical use, the CO_2 laser will be the laser of use for this thesis.

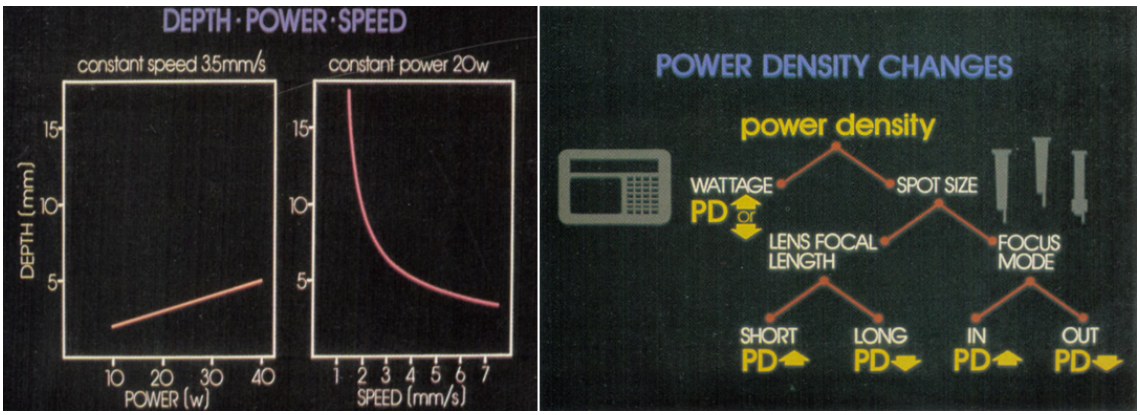

Figure 3.3: (Left) How power density and sweep speed affects laser cut depth. (Right) different parameters for effecting power density for surgical lasers. Reproduced from Atlas of CO2 Lasers [1]

In most surgical laser systems, the energy density of the laser cannot be directly controlled but it is instead regulated through the manipulation of a number of parameters, illustrated in Fig. 3.3. Regulating power or energy density in laser systems can be accomplished in multiple ways: altering physical technique of holding

the laser, altering the wattage, altering the laser mode. In those systems that use waveguides to direct the energy without distal focusing elements, the surgeon can further regulate the power density by altering the distal tip of the laser directing instrument to the target site. By changing the average wattage setting on the laser system, they can directly alter the average output wattage of the laser. By keeping other parameters constant, the surgical operator can change the power density of the laser by changing a single parameter, such as the Power setting on the laser surgical system, and enable deeper cuts as described in Fig. 3.3. Regulating these parameters to solve for a desired heat effect is not entirely straight forward as discussed in section 2.3. If a surgeon desires a 1 mm depth cut, how would they select their settings? How would a surgeon account for the differences in optical properties within the same tissue?

3.2 Current Methodology - Selecting Laser Parameters

If regulating laser parameters is not straightforward, then how do surgeons do it? Human surgeons certainly do not compute the complex differential equations discussed in 2.3.1 while in the operating room, and calculating the necessary parameters beforehand may be detrimental to the patient as the optical properties may be different from time to time [11]. If this is the case, how does one select their laser parameters?

To better understand this process, it can be useful to look at the training process for laser surgical procedures. Fig. 3.4 illustrates the generalized training for surgical laser operators, created from an interview conducted with a thesis committee member, Dr. Matthew Flegal, with clinical teaching experience. One must keep in mind

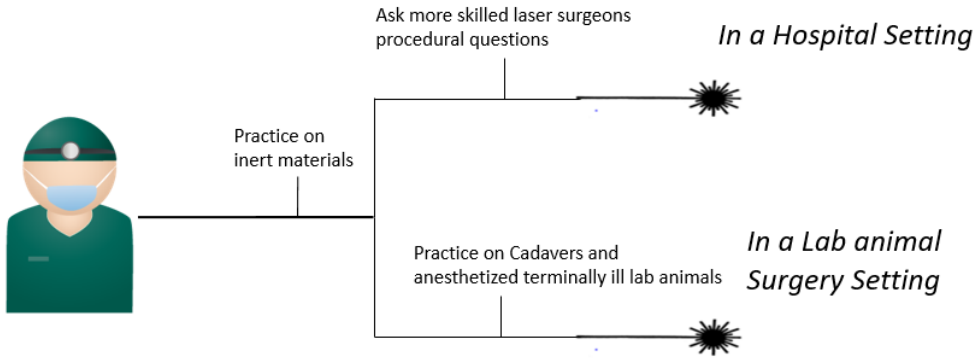

Figure 3.4: A generalized track on learning hand-held surgical lasers that diverges in methods based on learning environment.

the following information was put together from interviewing a single experienced source, and is subject to variation from surgeon to surgeon.

Both surgeons in the lab animal field and the hospital setting began training with inert objects with biological properties, such as fruit, chicken, pork shoulder, etc. The idea was mostly to learn how to navigate the fiber in a confined space but also to observe how the physical orientation can change and control the desired thermal effect. After the initial introduction into manipulating lasers, the two fields deviate. Those in the lab animal specialty will have more opportunity for hands on training with animal cadavers and terminally ill anesthetized lab animals, allowing them to observe the inflammatory response first hand. Those in the hospital setting would seek additional guidance from more skilled laser operators on how to perform the procedures, and shadow some of the procedures themselves before attempting one.

Now that there is a generalized understanding of the circumstances which surgeons learned how to use laser systems, let us comment on the thought process that goes on in the operating room. Based the interview conducted with Dr. Flegal, a few conditionals were isolated to describe the mental modeling that occurs for

individuals performing laser dissections or resections.

- The material properties of every tissue from every patient is different, so Surgeons are walking into each procedure with some unknowns [11].
- There is a desire not to perforate the tissue or cause a hemorrhage (ie, do not punch too deep to where the tissue cannot recover or cause excessive bleeding).
- Surgeons want to execute a laser resection with as little thermal damage spread as possible, minimizing the number of sweeps.

If we wanted to express the hypothetical model surgeons build in their mind using simplified mathematical notation, it could be described as:

$$DesiredDepth = f(LaserParameters - CautionFactor) \tag{3.1}$$

$$lim_{(Confidence \to \infty)} CautionFactor = 0 \tag{3.2}$$

$DesiredDepth$ refers to the desired depth the surgeon would like to execute with a single pulse or sweep of the laser. $LaserParameters$ refer to the optimal laser parameters, which at this point is unknown, used to achieve the $DesiredDepth$. $Confidence$ refers to the surgical laser operator's confidence level that selecting a higher power density laser parameters will not cause unnecessary damage. $CautionFactor$ has an inverse relationship with the $Confidence$ value and represents the caution the surgical operator has in selecting higher laser parameters.

For a surgeon to reach a $DesiredDepth$, they leverage their experience and the experience of others to formulate the $LaserParameters$ that would execute the procedure with minimum thermal damage spread. But as stated before, there are unknowns involved due to variances in the absorption media, non-homogeneity of the target, and biological variability around tissue. Because of these unknowns,

surgeons take some degree of caution going into the operation, represented above as $CautionFactor$. Taking this information and the conditionals into account, it is reasonable to picture an equation such as the one above where $DesiredDepth$ is equal to some function of $LaserParameters$ and $CautionFactor$ where as the surgeon increases $Confidence$ through observation of laser tissue interaction, the $CautionFactor$ approaches 0. Some surgeons apply interrogation pulses, depositing low amounts of laser energy but still enough to cause vaporization of the cellular material, and gauge the laser tissue interactions and depth using visual feedback. This in turn theoretically allows them to start building a correlation map of sorts to determine how they might augment the laser setting they had in mind before they start a resection procedure.

3.3 Modeling the laser pulse depth.

Based on the overview given above of how surgeons learn and perform laser cutting, we propose a novel approach to model a relationship between a laser parameter and laser pulse depth in biological tissue. We propose an approach where the laser first applies a few interrogation pulses, mimicking the surgical technique to build confidence, on the tissue and observes the resulting cutting depth to build tissue-specific models on-the-fly. This approach is inspired and motivated by the observation of experienced laser surgeons in their practice: before deciding what laser parameters to use, they often apply a number of laser pulses and observe how the tissue reacts. Our aim is to automate this process and provide a tool that learns these relationships on the fly, as a surgeon would. We propose to use a robot to consistently and repeatedly manipulate the laser fiber to deposit the same energy density on tissue, and the use of statistical regression techniques, in combination with image

processing algorithms, to observe the laser pulse depth and rapidly build a model capable of predicting the pulse depth.

Chapter 4

Modeling the laser ablation process

This chapter focuses on the formulation of hypotheses concerning modeling the laser ablation depth with a single pulse (laser pulse depth) and the materials and methods used to test out the hypotheses.

4.1 Problem formulation

In this thesis, we formulate the problem of modeling and predicting the laser ablation depth using methods and concepts from statistical regression theory. As we have seen in section 2.3.1, the beam intensity and power distribution of the laser cannot be directly prescribed, but it is instead regulated through the selection of the several operational parameters. Inspired by how surgeons perform laser cutting, we wish to mimic their ability to manipulate and model the effects of the laser parameters:

- the **power** level P, i.e. the total energy flowing through the beam in unit time. There is a relation between this parameter and the beam intensity I at any

cross-section $\hat{z}$ along the optical axis: $P = 2\pi \int_0^{+\infty} I(r, \hat{z}) dr$.

- the laser **spot size** w_z, as it was defined in section 2.1.2 and 2.1.3. Conventionally, the spot size is measured at the surface of the tissue, i.e. at $z = 0$.
- the **time of exposure** τ, which is defined as the amount of time for which the laser output is enabled.
- the **beam velocity** v relative to the tissue surface. For a stationary laser beam, $v = 0$.

We wish to explore models that map the laser parameters outlined above to the resulting ablation depth.

4.1.1 Hypothesis 1: Modeling the Ablation Depth as a Parametric Function of the Laser Parameters

We hypothesize that, for any given combination of laser wavelength and tissue type, a function f exists that models the mapping between the vector of laser inputs $\mathbf{u} = [P, w, \tau, v] \in \mathcal{U}$, with $\mathcal{U} \subset \mathbb{R}^4$, and the resulting laser ablation depth:

$$d = f(\mathbf{u}) \tag{4.1}$$

We further hypothesize that the function f can be approximated using the following parametric model:

$$\hat{f}(\mathbf{u}) = \mathbf{w}\ \phi(\mathbf{u}) \tag{4.2}$$

where d is the laser ablation depth depth, $\phi(\mathbf{u})$ is a 5-dimensional column vector of basis functions $\phi_j(\mathbf{u})$ with $\phi_1(\mathbf{u}) = 1$, and $\mathbf{w}$ is a vector of regression coefficients. To study the validity of this hypothesis, we propose to (1) collect experimental data, i.e.

a dataset consisting of L data pairs $\{d^i, \mathbf{u}^i\}_{i=(1,\ldots,L)}$, (2) select a family of suitable basis functions ϕ_j, and (3) estimate the vector of parameters $\mathbf{w}$ with an appropriate learning algorithm. Execution of these three tasks will be described in detail in the next chapter.

4.1.2 Hypothesis 2: Building Tissue-Specific Ablation Models On-the-Fly

We hypothesize that an equation $d = \hat{f}_L$ exists where $\hat{f}_L$ is trained using regression techniques from data sets of $[\mathbf{u}_l, d_l]$ to predict for data pairs $[\mathbf{u}_L, d_L]$ where d, d_l, d_L are corresponding maximum ablation depth measurements, $\mathbf{u}_l, \mathbf{u}_L$ are the corresponding laser settings described in hypothesis 1, and $\mathbf{u}_l < \mathbf{u}_L$.

The model building protocol involves using data from less powerful laser pulses, in terms of power density, to predict for data using more powerful laser pulses. To accomplish this, all laser parameters in vector $\mathbf{u}$, defined in hypothesis 1, will be kept constant with the exception of one parameter which will remain an independent variable. The selection of this parameter will be determined in section 4.2.3. This protocol is inspired by how physicians estimate laser parameters for soft tissue laser dissection using low laser settings to minimize tissue damage.

4.2 Materials

In the remainder of this chapter we describe the materials used to collect experimental data. Based on background information from chapters 2 and 3, there are several design constraints for the experiment: 1) selected parameters for building predictive model must change two dimensional power density of the laser pulse, 2) samples used for testing must be from the same type of tissue and from the same

donor in order to limit the effects of biological variability [11], 3) must be able to extract as many samples as possible from aforementioned tissue.

Specifications of equipment used in these experiments (Panda Robot, FLIR Thermal Camera, LEICA Cryotome) can be seen in Appendix A.

4.2.1 Tissue Sample and Preparation

The tissue model used in this study is chicken breast. Although it may not be representative of every type of soft tissue that may be found in clinical practice, chicken breast was selected because it is easy to procure and has been used in another laser ablation study [15]. Chicken breast also presents challenges similar to those encountered in soft tissue laser surgery: 1) the orientation of the fibers affects the structural and thermal properties, 2) the orientation of these fibers was unknown during and after laser action, 3) the denaturation of proteins in the thermal damage zones surrounding the ablation crater induces stress in the tissue (the kinetics of which are largely unknown) [12]. A tissue inflammatory response might pose a risk in changing the ablation profile of a laser surgical cut, but because the cells in the chicken breast tissue were already killed via food processing and freezing variation from tissue inflammation will not be represented in this experiment [16].

We used the following protocol for the preparation of tissue samples. The chicken breast was kept frozen prior to testing. The whole chicken breast was removed and laid on a table or cutting board with the anterior side facing up. An 8 mm biopsy punch, "biopunch - 8" made by Ted Pella Inc., was pressed into the anterior surface of the still frozen chicken breast. The result of the procedure was cylindrical shaped tissue samples. Before performing laser experiments, tissue samples were kept in a warm water bath kept at 28-30 degrees C to bring samples to just above room temperature and to keep the tissue hydrated. The water bath was prepared

using a scientific heating plate and a calibrated thermometer to measure the water temperature. The chicken temperature was measured after it was placed in the water using an FLIR Thermal imager, allowing for non-invasive measurements. Because the samples have such low mass, it generally took less than 2 minutes to bring it up to temperature. It is anticipated with this setup that most samples will fall within 2-3 degrees C of the median. Some heat loss is expected once the tissue is removed from the water bath. It is important to keep the temperature range small in the samples to mimic the human body's ability to keep most tissues within a few degrees from 37 C. As such if the tissue has remained out of the bath for more than 1 minute, it is instructed to place it back to bring up to room temperature.

4.2.2 Benchtop setup

For the design of the experiment, the following assumptions were made:

A 7-axis robot from Franka Emika (Munich, Germany) was used to manipulate the laser waveguide. This robot used a custom end effector seen in Fig. 4.1 to grasp and use the laser waveguide.

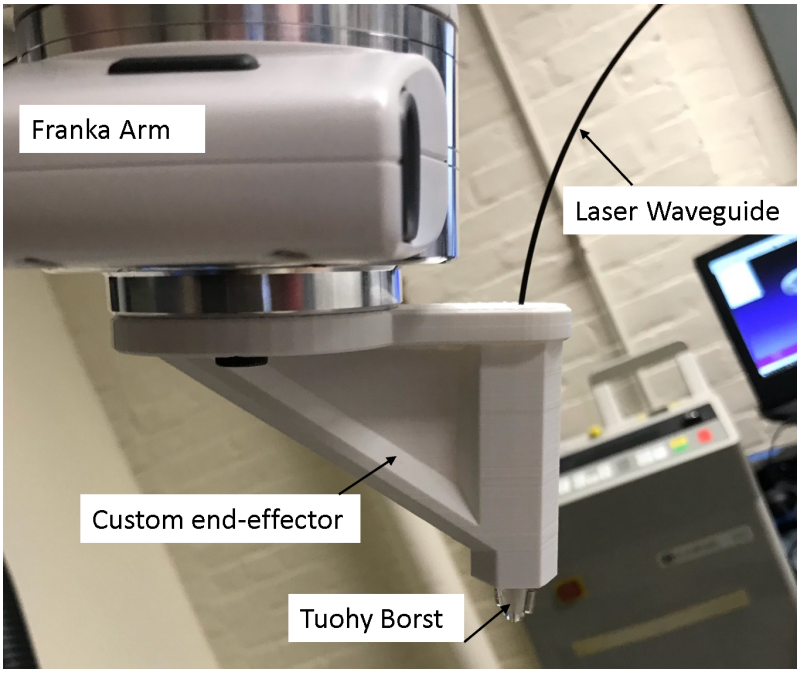

Figure 4.1: Custom end effector with components labeled

4.2.3 Laser System

The laser system being used in this study is the Lumenis-30C, a CO_2 laser system (wavelength: 10.6 μm max power of 30 Watts) [8]. This system has an internal, vertical optical cavity with a "proprietary mixture of gases" for the CO_2 laser medium, as well as an internal laser testing mechanism to ensure proper operation during the procedure [8]. It allows for change of the laser mode, the tissue target exposure mode, the time on/off for the laser, and the average power of the laser [8]. To influence the spot size of the laser, the surgeon would need to change the distance from the fiber tip to the tissue by hand [1, 8, 9]. We will describe the laser parameters that come with the laser system, and select which parameter will remain an independent variable while the others remain constant.

Laser Modes There are three primary laser modes available through the Lumenis 30C: Continuous wave, Pulser, and Super Pulse [8]. The Super Pulse setting is characterized in Fig. 4.2.

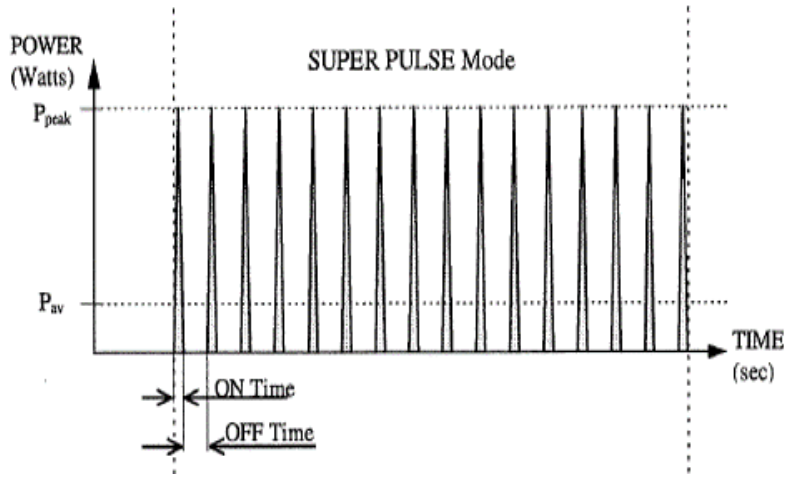

Figure 4.2: Graph of energy delivered from Super pulse as a function of Power, time on, and time off. Reproduced from Lumenis 30C User manual. [8]

Continuous wave, as the name suggests, is a laser emitted at constant power for the entire duration of the laser action. Pulser is repeated laser pulses at a continuous power. Energy delivery in Super pulse is characterized by a function where power ramps up to a high power that is significantly larger than the average power and then ramps down. Short pulsed modes like super pulse have been shown to minimize thermal spread, according to the Lumenis 30C instruction manual [8]. This mode is most likely to be used in laser dissection and laser resection procedures, according to a journal publication on resection of benign eyelid tumors using Super Pulse CO_2 lasers, which is why **Super Pulse** will be the selected laser mode for this thesis [13].

Power Setting The Power setting, according to the manual, refers to the average power emitted by the laser. For each of the modes, except for continuous wave, the surgeon would need to calculate the average power, if they desired. In the manual, it states that Super pulse with a Power setting of 0.5-5 W would be optimal for "Bulk Vaporization," where Surgeons kill a tissue target using thermal damage and vaporization, and it states that Super Pulse with 5-10 W would be more optimal for laser dissection or laser resection procedures [8]. For the purpose of this thesis, will be modeling how power affects laser pulse depth, and limiting the range of power for experimental data collection to 5-10 W.

Tissue Target Exposure Tissue Target Exposure modes refer to the way the target receives the laser energy, and while it may use similar terminology it does not determine the laser modes described earlier. For example, a beam emitted constantly is classified as continuous exposure, where the laser is on as long as laser activation is occurring, and can be performed using all three laser modes (Continuous wave, Pulser, and Super Pulse). Single Pulse Exposure, which refers to exposing the laser for a singular period of time that the user can set in the console, and repeated exposure, which refers to exposing the laser for multiple laser pulses where the user can input settings for frequency of repetitions [8]. To minimize thermal damage spread for a laser dissection/resection, most surgeons select the repeated exposure or single pulse settings. On the other hand, Continuous would be more optimal for procedures where higher thermal damage spread is desired [8]. Because the subject of the thesis is attempting to model depth from a single pulse, **single mode** will be used for the experimental procedure.

Time settings On the Lumenis 30C, "Time on" and "Time off" refer to the time the laser is firing a pulse and the time in between each fired laser pulse. Both settings

apply for any repeated Tissue Target Exposure, and only "time on" applies to single pulse exposure [8]. Charring on the samples was desired to provide additional visual feedback during data acquisition. During preliminary testing, fissures on the tissue surface were mistakenly identified as the ablation crater. With some preliminary experimentation, it was determined that "time on" of 0.2 seconds would be used for the thesis.

4.3 Methods

Having introduced the components of our setup, we now describe the experimental protocol we developed to perform controlled laser ablations and measure the corresponding ablation depth.

4.3.1 Experimental Protocol

All necessary laser safety guidelines were followed, such as having the fume extractor on during laser experiments, and proper safety equipment worn during the procedure. Prior to the experiment, tissue was prepared in a warm water bath using the protocol listed in section 4.2.1. Tissue was kept in the water bath and monitored using an FLIR thermal imager until the laser was ready to fire and the robot was in position.

1. The Lumenis 30C was turned on using the following laser settings: Single Pulse, Super Pulse, and Time-on = 0.2 seconds. Power was determined on a sample by sample basis. The reasoning behind these selected laser parameters was explained in section 4.2.3.

2. The laser waveguide was attached to the Lumenis 30C with the distal end fastened into the robot end effector seen in Fig. 4.1.

3. Afterwards, the robot end effector was zeroed on the analysis fixture, over where the sample will be placed seen in Fig. 4.3. This ensures that the robot knows how to assume poses relative to the tissue location.

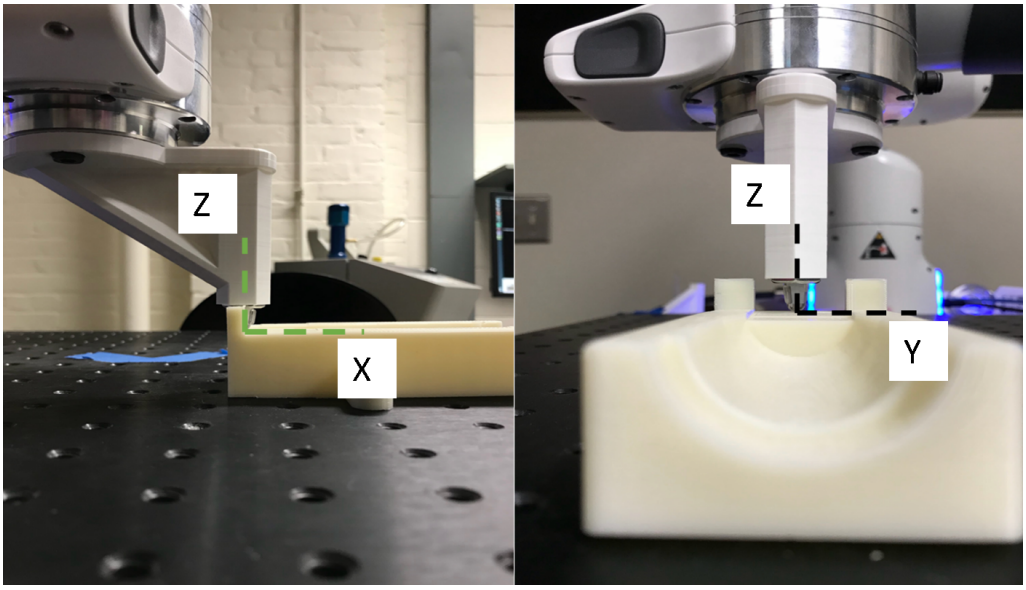

Figure 4.3: Robot end effector remembers this point and associates it as the zero position in the X,Y,Z axes

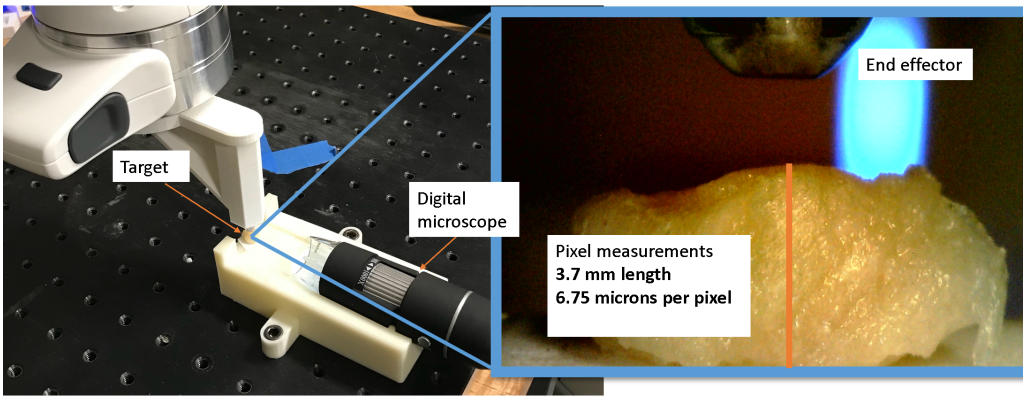

Figure 4.4: Tissue target is measured to ascertain the height, Robot moves to be 2 mm + the tissue target's height above the zeroed point

There is a 1 minute window to complete the next 5 steps and perform a laser action after the tissue sample is removed from the water bath. If too much time has elapsed, the tissue sample should be brought back to temp, and the procedure should restart here at **step 4**.

4. After moving the end effector away, the tissue sample was removed from the bath and placed on the analysis fixture on the previously zeroed spot.

5. Using a portable microscope camera (VSATEN3) measurements were taken of the tissue length in the z direction using pixel measurements.

6. The robot was commanded to assume a pose where the end effector is 2 mm + the newly measured height of the sample above the zero point.

7. The thermal camera (FLIR A655sc) acquires a non-invasive temperature measurement of the sample before laser action.

8. The robot and the laser operator give the command for laser action and fires a laser pulse at the target. A fume extractor was used to remove any tissue particulate from the air, as is required by laser safety protocols.

9. The tissue was then placed in a compliant tray without directly interfering with it and then frozen using an optimal frozen sectioning compound from Sakura Tech

10. Repeat steps 4-10 using remaining samples in the heated water bath. For this experiment, sample groups of 10-12 samples were laser pulsed and frozen.

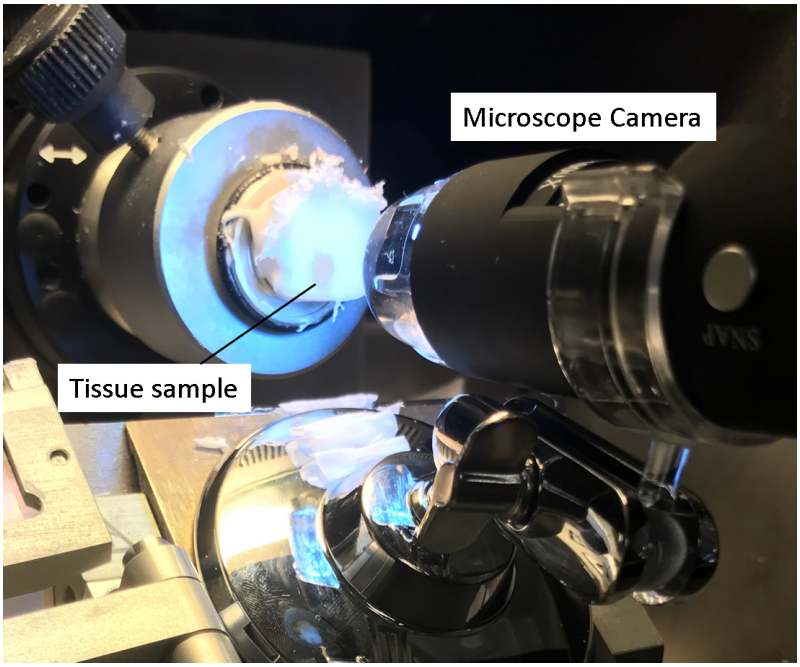

Figure 4.5: Cryotome slicing and imaging setup

When the sample(s) were frozen properly in the OCT fluid, they were taken to a Leica cryotome for slicing and imaging. The VSATEN portable microscope was outfitted with a yellow filter, and portable UV light was placed inside the cryotome to illuminate the sample. The cryotome setup described above, seen in Fig. 4.5, works by keeping the cutting tool fixed, and moving the sample closer and down over the tool. Taking advantage of this feature and the micron accuracy this machine has in bringing a sample back to the same plane, we are able to set up a digital microscope to observe the tissue and the laser ablation profile. During slicing, the portable digital microscope with a yellow filter takes pictures of the front face of the sample after every slice. The UV light fluoresce and enhance the profile of the cut while the yellow filter enhances the image further, significantly increasing contrast on the digital microscopic images. The UV light fluoresces what appears to be thermally damaged tissue in laser

ablated chicken breast. But it is unknown what fluorophores are reacting to the light, and it is unknown if they are exclusive to thermal damage, although they initially appear to be at least for the chicken breast. As such, UV excitation was not enough to identify an ablation zone, and charring on the surface of the tissue was necessary to identify where the ablation zone starts.

11. Sample(s) were trimmed down using 50 micron slices until evidence of laser tissue interactions were noticed using a two-step verification. 1) Char must be present on the surface of the ablation, 2) there must be a clear ablation profile, usually enhanced by a green glow.

12. Once seen, 50 micron slices were taken and images of the face of the sample after each slice.

13. Slices were taken throughout the ablation profile and images were acquired using the portable microscope camera, total of one image per slice.

14. Data was recorded for outliers, if the sample seemed to slip out and break, or the ablation profile looked non uniform.

15. Data was recorded for slice thickness from the start of the ablation profile. If slice thickness changes, mark it in the notes. It is imperative to record the distance traveled by the sample while slicing (ie. the slice thickness for each slice) for data analysis later.

Using imageJ, pixel measurements were taken for maximum depth in each slice of the ablation profile for every 0.05 mm slice and plotted. Gaussian fit models were constructed for each sample's ablation profile. Specifications and information on the Thermal Camera and Cryotome used can be found in Appendix A.

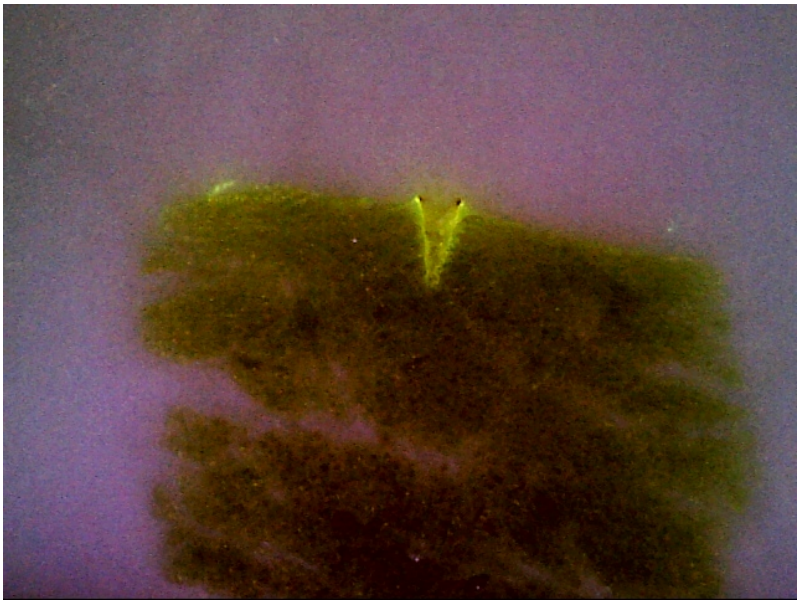

Figure 4.6: Sliced face of the tissue sample, UV Fluorescent lighting highlights area with thermal damage

4.3.2 Data acquisition

Using the assumption that one can plot a 2D view of the ablation profile along a Gaussian-like curve, using the total number of slices multiplied by the slice thickness as the X and maximum depth recorded for each slice as the Y. Once sectioned and imaged, the depth of the ablation at each slice was measured using pixel measurements (ImageJ). The Gaussian equation for fitting data collected from the images are as follows

$$f(x) = ae^{(\frac{-(x-b)}{c})^2} \tag{4.3}$$

where the parameter a is the peak for the Gaussian fit of the laser ablation, which in this case is representative of the maximum depth of our ablation crater. The a parameter in the Gaussian equation is recorded for each sample and fed into the regression model.

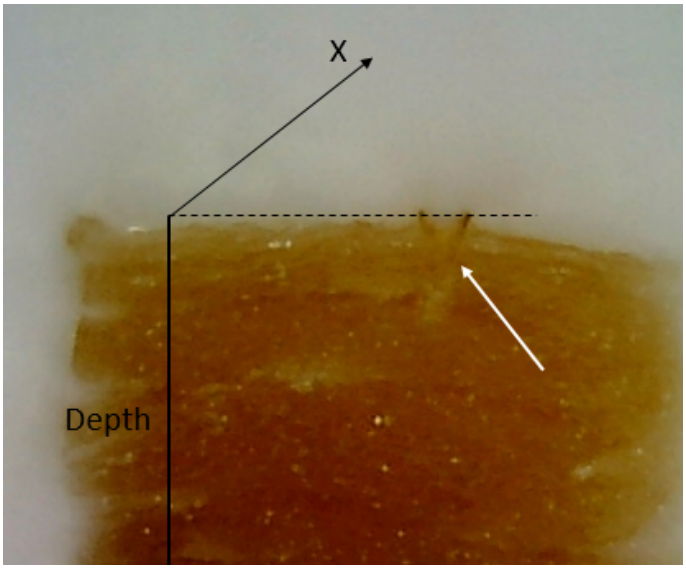

Figure 4.7: One slice of the tissue sample, slicing in the positive X direction and extracting depth of pulse per slice in the Y direction

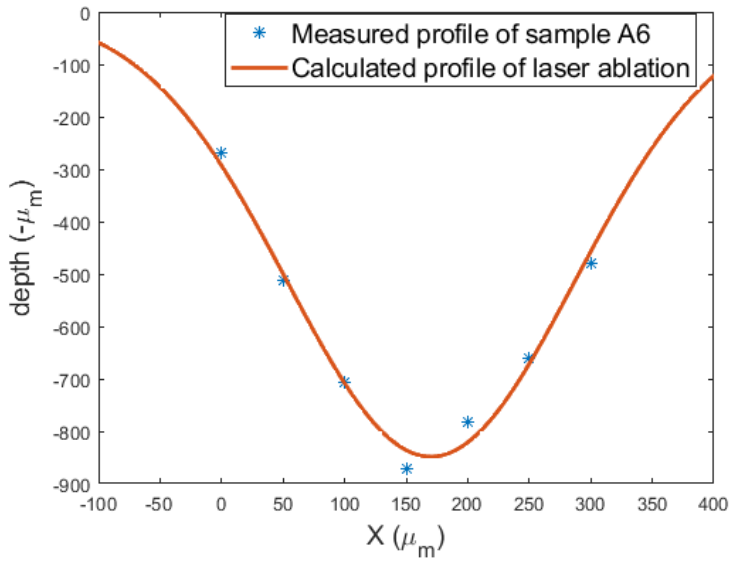

Figure 4.8: Gaussian fit for slice profile of the tissue sample in the previous figure, X is the slicing direction and Y is the depth

4.3.3 Regression Modeling

Supervised learning is an appropriate solution for trying to model phenomena that are difficult to describe in closed analytical form [17]. Regression learning is one such method used to create estimation models based on observed data [17]. The proposed method is to use regression techniques to model the relationship between the variable laser parameter, Power, and laser pulse depth using multiple techniques.

The proposed model building techniques treat the tissue and the laser system as black boxes and try to glean estimation curves to help predict what laser power setting should be used. When comparing models for general data analysis experiments, one would take data points at random to train or build a model and take the remaining data points to run statistical tests to validate the model (hypothesis 1). This procedure may not reflect well in clinical practice where the physician would prefer to use only lower power levels to build their mental model. A more clinically relevant procedure would be to train these models on data points below a certain power threshold and validate them on the data points above the threshold, mimicking the surgical technique (hypothesis 2). Temperature data was collected to use as criteria for supervision techniques. The models may be refined using data exclusion or multi-variable regression using temperature and power. The criteria on which data can be excluded based on temperature values will be determined by the total distribution of temperature values for the collected data.

The regression modeling workflow is as follows:

- Observe the total data and temperature data. Hypothesize an equation that describes the trends observed.
- Perform regression to fit the equations to the data and compare them.
- Perform temperature based data exclusion, or multi-variable regression.

- Train and validate the models using randomized data points from the total data and the temperature filtered data. -Hypothesis 1
- Train the models using data points below a power threshold and validate using data points above the power threshold.

Each method for the regression techniques are described in their corresponding results section.

Chapter 5

Results and Discussions

In this chapter, we report on the collection of experimental evidence aimed to test the two hypotheses formulated in section 4.1. An initial set of experiments was conducted to explore the range of laser inputs and inform our experimental design. Exploratory data analysis was performed to inform the selection of basis functions for the regression. The resulting models were compared via goodness of fit metrics: degrees of freedom (DFE), R^2, Root Mean Square Error (RMSE), and Validation Root Mean Square Error (V RMSE).

5.1 Initial Data Collection

Excluding preliminary data collected to build better procedural protocol, fifty-seven samples were collected over five testing intervals. As outlined in the procedure in chapter 4, only Power (as reported by the laser system) and laser pulse depth are measured, and all other parameters (time on, Super Pulse, 2 mm distance from target) are assumed constant. The range of the input Power is 0-10 W, but data for Power levels less than 5 W were difficult to collect reliably due to an absence of charring. In section 4.3.1, it was explained why charring was necessary to identify

an ablation zone. The laser ablations for power levels less than 5 watts were so small and left behind little to no charring that it was difficult to differentiate them from the fissures on the surface of each sample. Additionally, the manual for the laser system instructed that laser surgical operators use power settings of 5-10 Watts for the purpose of laser dissection, as described in section 4.2.3. As a result, only data from Power levels of 5-10 W were used for the experiment. This section details the total results and distribution of the data. 57 total data points were collected following the procedure outlined in chapter 4.

5.1.1 Results: Power vs Incision Depth

The scatter plot for the total data shows a positive proportional relationship between Power level and laser pulse depth.

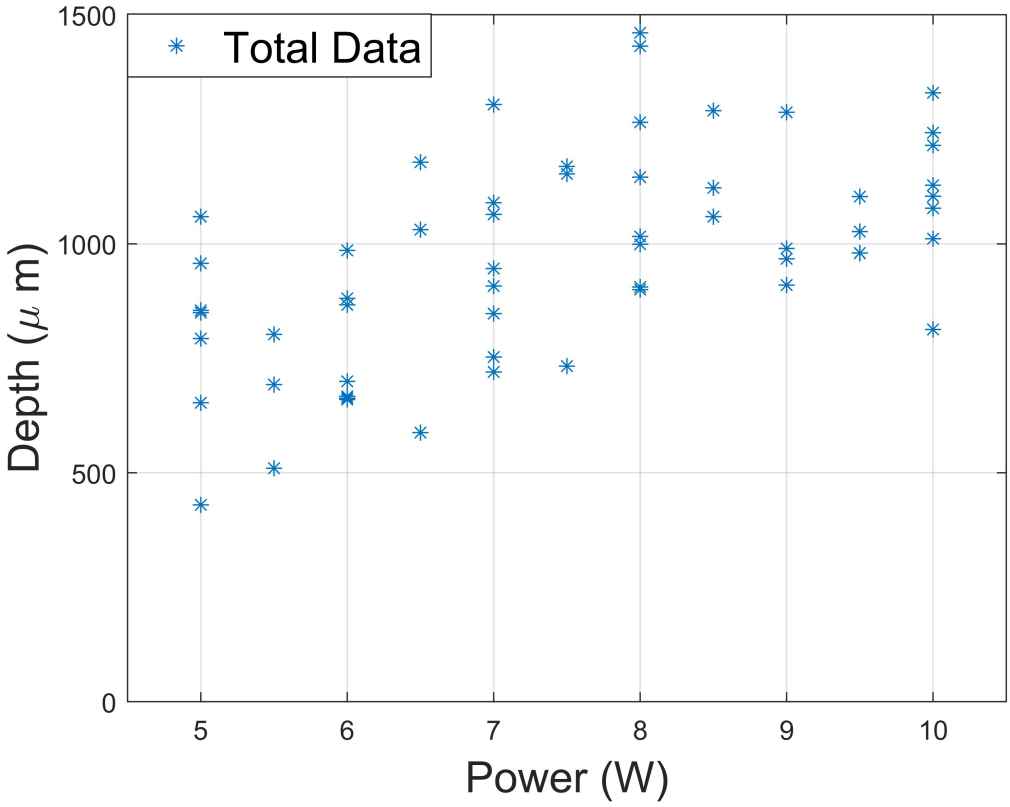

Figure 5.1: Scatter plot of the total data for Power and Laser Pulse Depth

We first performed a One-Way analysis of variance (ANOVA) to test the hypothesis that the data shown in Fig. 5.1 could be simply explained by a simple intercept model. We tested the null hypothesis H0: $d = Pb_1 + b_0, b_1 = 0$, with alternative hypothesis $b_1 \neq 0$. The F-Test rejected the null hypothesis with p-value $4.206 \cdot 10^{-6}$, showing statistical significance between Power, as reported by the laser system, and laser pulse depth. We understand that this is only a portion of the truth, that the ablation depth is more dependent on the power density of the laser and not just the power [7].

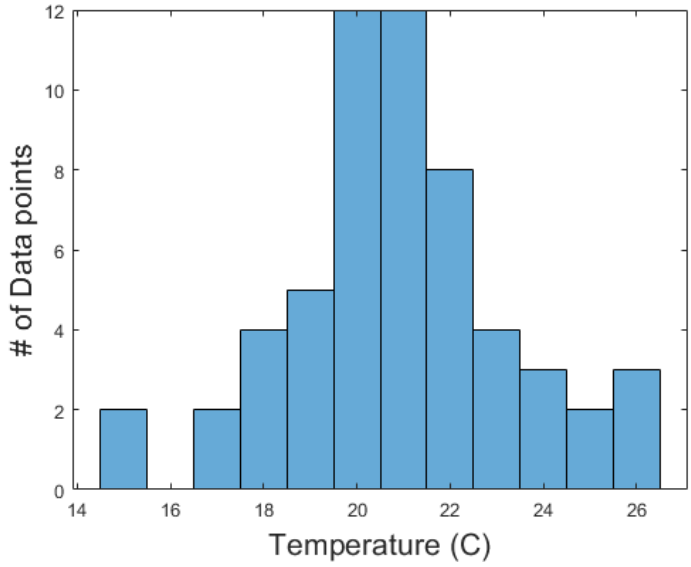

Figure 5.2: Temperature data histogram

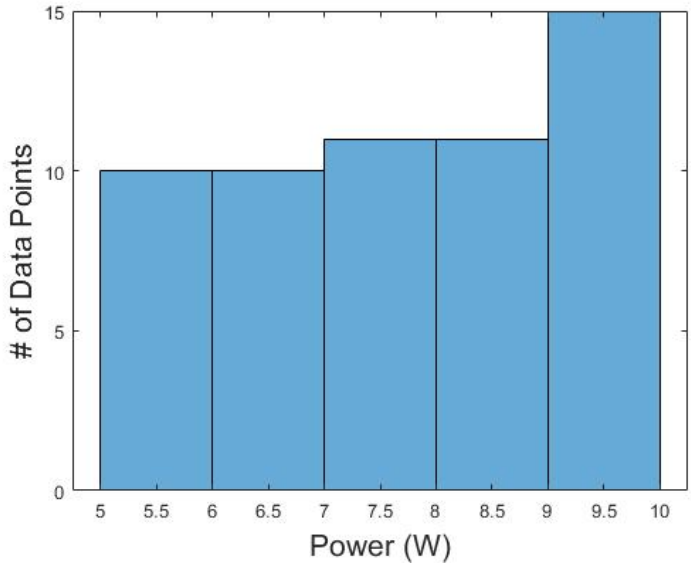

Figure 5.3: Power data histogram

5.1.2 Discussion

The scatter plot and the one-way ANOVA test revealed an upward trend between power as reported by the laser system and laser pulse depth. We understand that this is only a part of the truth, as the literature points out that the relationship is between power density and laser pulse depth, which can be changed using the power setting [7]. The laser pulse depth seems to taper off after 8.5 W. Because the tissue and the laser surgical system is being treated as "black boxes", it is unclear if this observed effect is rooted in the tissue properties or the laser system output.

The Power histogram from Fig. 5.3 shows that the data distribution was not perfectly equalized, which would lead to higher power data points carrying more weight in the models. Unexpected behavior was observed early on in the higher power level data points, and more experiments were performed to ascertain if those data points were outliers or not. Temperature data was also recorded for the purpose of verifying the experimental conditions were met. It was found that the temperature distribution was larger than what was experimentally desired in section 4.2.1. It is hypothesized that the constant airflow from the fume extractor, coupled with varied execution times for each sample (time from removing the sample from a water bath to performing laser action), may have lead to this large variance in sample temperature before laser action, seen in Fig. 5.2. It was found through statistical testing that samples with different recorded temperatures had significantly different depth measurements and might explain much of the variance seen in the plots. the models might benefit from incorporating temperature into the predictive models or excluding data based on the temperature distribution curve, excluding data points where temperature is less than 20 C and greater than 22 C. This criteria was selected because 32 out of the 57 data points resided in this range. This is further explored in section 5.2.1.

5.2 Model Selection

This section contains the experimentation involved with building different models and comparing their goodness of fit metrics: RMSE, V RMSE, and R^2. The goal is to select the model with the best capability for estimating depth and to explore solutions involving Multi-variable regression with Temperature and Power as well as explore the effectiveness of data exclusion using temperature values as the criteria.

Visual interpretation of the data in Fig. 5.1 seems to suggest a positive relation between the laser power and the ablation depth. We use two possible models for statistical regression (linear and logarithmic) detailed in the next section.

5.2.1 Results

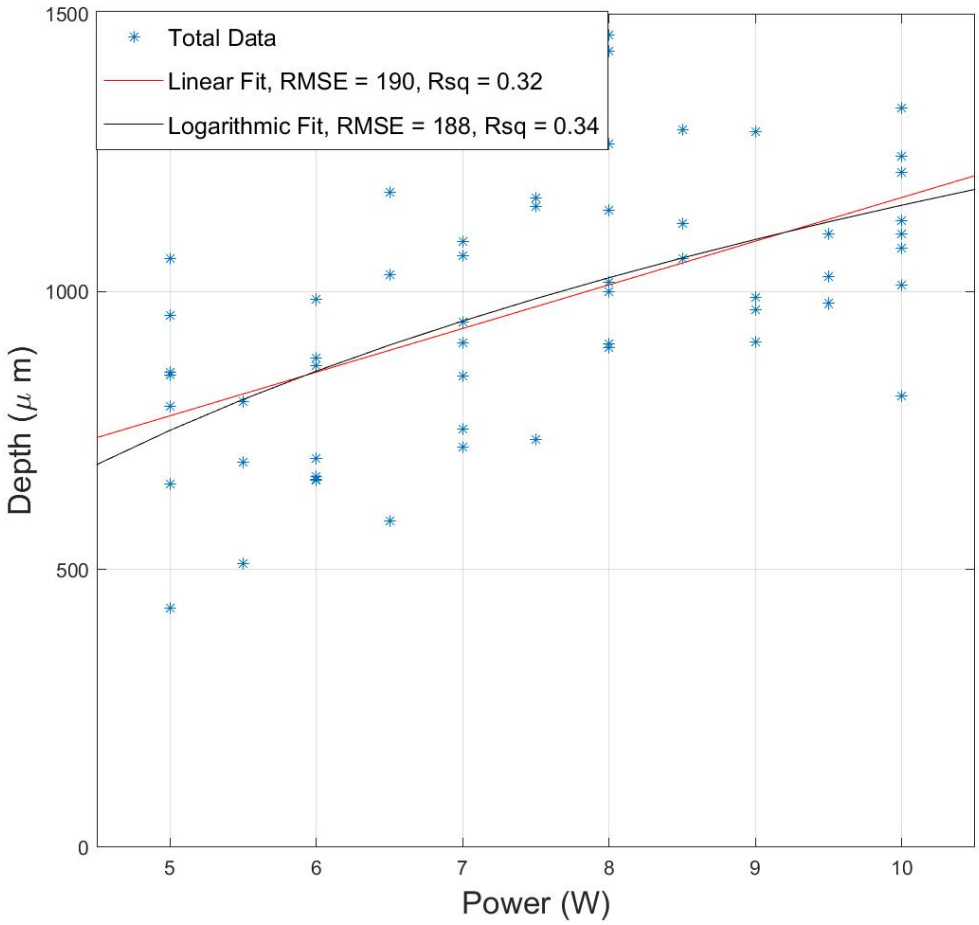

Figure 5.4: Linear fitted model (RMSE = 190, Rsq = 0.32) compared to logarithmic fitted model(RMSE = 188, R squared = 0.34)

Table 5.1 displays the results of linear models generated using random data points from the total data using this equation:

$$\hat{D} = b_1 P + b_0 \tag{5.1}$$

and comparing the models generated with the rest of the data as validation data, where $\hat{D}$ is the estimated depth, P is the power level of the laser, b_1 and b_0 are coefficients. The method of selecting random data points for training and validation was performed five separate times with training and validation size of 28 data points each.

The confidence interval for the validation RMSE values is [175,214] μm. Table 5.2 displays the results of logarithmic models using random data points from the total data using this equation:

$$\hat{D} = b_1 ln(P) + b_0 \tag{5.2}$$

and comparing the models generated with the rest of the data as validation data, where $\hat{D}$ is the estimated depth, P is the power level of the laser, b_1 and b_0 are coefficients.

The confidence interval for the V RMSE values is [175,214] μm.

Because of the large variance observed in temperature recordings, linear and logarithmic models were explored to see if temperature values can help explain some of the unexpected behavior seen in the total data, Fig. 5.1. Below are the results

Table 5.1: Goodness of Fit metrics for linear models trained and validated using randomly selected data points.

Fit Name	R^2	DFE	RMSE (μm)	V RMSE (μm)
Rand1	0.41	26	193	190
Rand2	0.41	26	168	209
Rand3	0.27	26	201	183
Rand4	0.47	26	163	213
Rand5	0.25	26	205	177

Table 5.2: Goodness of Fit metrics for logarithmic models trained and validated using randomly selected data points

Fit Name	R^2	DFE	RMSE (μm)	V RMSE (μm)
Rand1	0.46	26	187	190
Rand2	0.44	26	163	209
Rand3	0.28	26	199	183
Rand4	0.46	26	166	213
Rand5	0.28	26	201	177

when incorporating Temperature values, T, into the models using these equations.

$$\hat{D} = b_1 P + b_2 T + b_0 \tag{5.3}$$

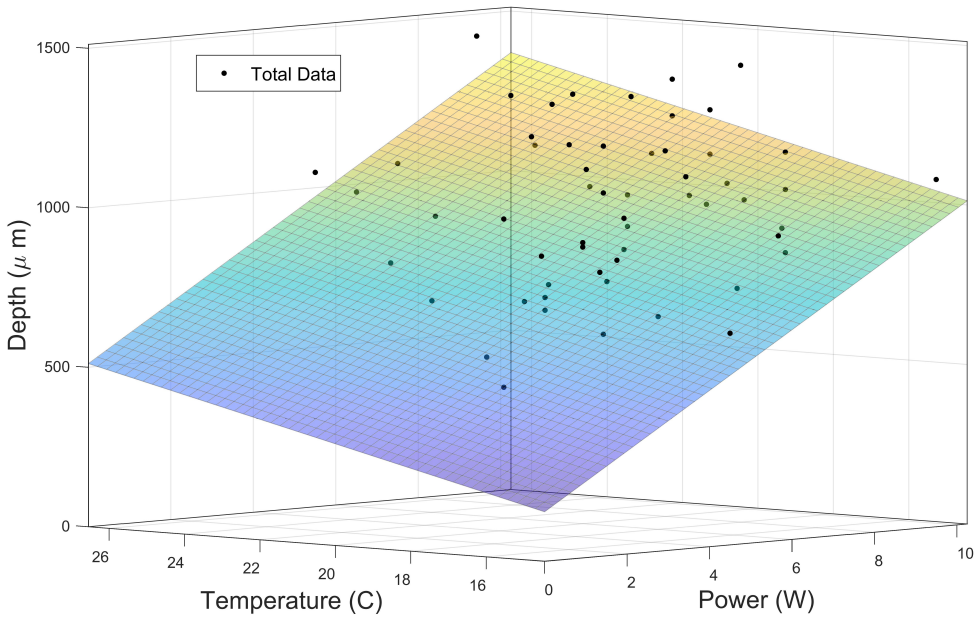

Figure 5.5: Linear fitted planar model (RMSE = 177 μm, Rsq = 0.42)

$$\hat{D} = b_1 ln(P) + b_2 T + b_0 \tag{5.4}$$

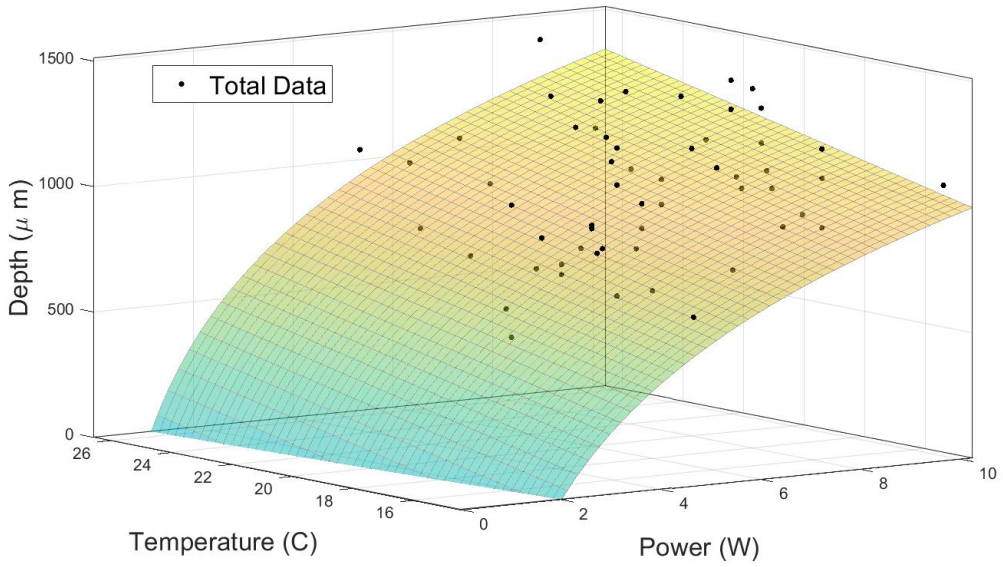

Figure 5.6: Logarithmic fitted model(RMSE = 176 μm, R squared = 0.43)

Data exclusion using temperature as a criteria, all data outside T = 21 +/- 1 C, was explored as a possible solution to create better predictive models. This criteria was selected because 32 out of the 57 data points resided in this range. Below are the results when excluding data based on temperature criteria.

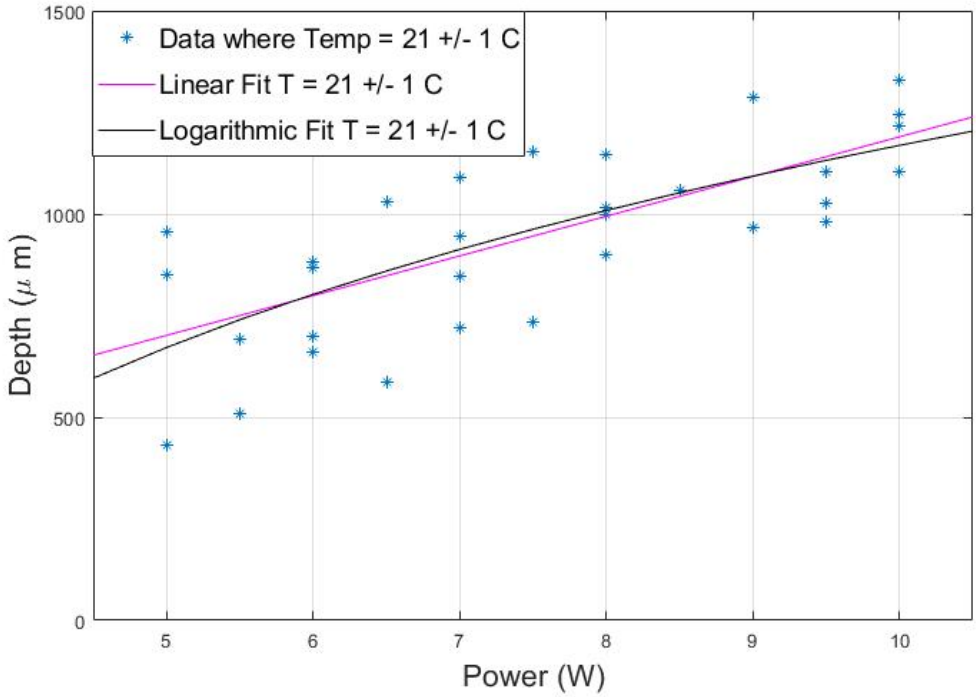

Figure 5.7: Plot of included data based on parameters of Temperature = 20 to 23 C. Linear fitted (RMSE = 162, R square = 0.5) vs Logarithmic fitted (RMSE = 163, R squared = 0.5)

Table 5.3 displays the results of linear models generated using random data points from the Temperature filtered data using this equation:

$$\hat{D} = b_1 P + b_0 \tag{5.5}$$

and comparing the models generated with the rest of the data as validation data, where $\hat{D}$ is the estimated depth, P is the power level of the laser, b_1 and b_0 are coefficients.

Table 5.3: Goodness of Fit metrics for linear models trained and validated using randomly selected, temperature filtered data points

Fit Name	R^2	DFE	RMSE (μm)	V RMSE (μm)
Rand1	0.55	14	185	151
Rand2	0.44	14	176	143
Rand3	0.56	14	130	187
Rand4	0.46	14	188	135
Rand5	0.55	14	112	202

The 95% confidence interval for the validation RMSE values is [127,200] μm.

Table 5.4 displays the results of logarithmic models using random data points from the Temperature filtered data using this equation:

$$\hat{D} = b_1 * ln(P) + b_0 \tag{5.6}$$

and comparing the models generated with the rest of the data as validation data, where $\hat{D}$ is the estimated depth, P is the power level of the laser, b_1 and b_0 are coefficients.

Table 5.4: Goodness of Fit metrics for logarithmic models trained and validated using randomly selected, temperature filtered data points

Fit Name	R^2	DFE	RMSE (μm)	V RMSE (μm)
Rand1	0.59	14	176	164
Rand2	0.46	14	173	154
Rand3	0.53	14	134	186
Rand4	0.46	14	189	135
Rand5	0.54	14	113	201

The 95% confidence interval for the validation RMSE values is [135,200] μm.

A paired T.test was performed on the V RMSE values for the linear fit and the logarithmic fit for the Temperature filtered data, with an $\alpha = 0.05$. The results showed that there was not a significant difference, with a p.value of 0.07.

5.2.2 Discussion

Both the linear and logarithmic models built from the total data have comparable metrics, with the logarithmic fit being marginally greater. It might possibly be due to the curve like behavior observed in Power levels greater than 8.5 Watts. One of the limitations of this study is that we have no hard evidence of how our models could perform outside of the range of inputs used for training, i.e. outside of the 5-10 W range. The logarithmic model predicts no ablation at less than 2 Watts, we have some evidence to show this is not necessarily true in Fig. 5.8, and the linear model states ablation occurs at 0 Watts which we understand to be impossible.

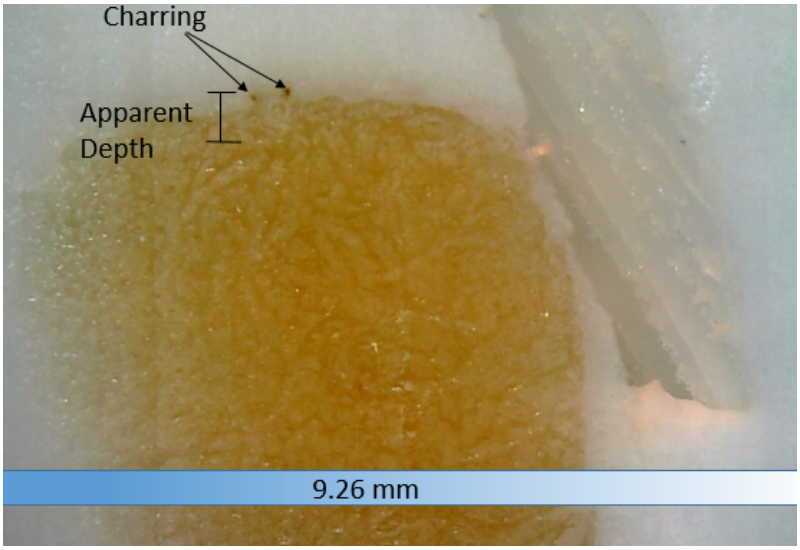

Figure 5.8: A slice of a preliminary sample that has been ablated using 2 W single laser pulse, Super Pulse setting. **NOTE:** Not part of the experimental data

When temperature was introduced into the model for plane fitting, higher R^2 values and lower RMSE values were achieved, showing that the temperature differences may explain some of the variance observed. Seeing this, data exclusion was introduced based on the total temperature distribution in Fig. 5.2.

Data that did not fall in the temperature range of 20-22 degrees C was excluded, the remaining data referred to from here on as "temperature filtered data," and allowed for models with higher R^2 values and lower RMSE values. The temperature filtered data was tested by selecting random data points to train a model and random data points to validate against. This was done five times each for both linear fits and logarithmic fits, and the results are comparably better in terms of V RMSE when compared to their counterparts from the total data. When looking at temperature filtered data, the linear fits appear to be the better models with a lower mean V RMSE and lower confidence interval for V RMSE. The paired t.test shows that though the data sets are different, they were not significantly different enough to

pass a 95 percent t.test.

5.3 Learning models on the Fly

It was touched on in section 4.1.2 that validating the model off of random data points may not be as clinically relevant as other methods for model generation. In current practice, a surgeon uses low power levels to estimate the laser tissue interactions with the assumption that their desired power setting is higher. In essence, they estimate the depth v power relationship for higher power levels using multiple low power level interrogation pulses. This section goes over model generation using lower power levels and validates using the remaining higher power levels.

5.3.1 Results - Learning Models on the Fly

Fig. 5.9 and Table 5.5 show the results of linear models trained using power levels below a moving threshold value and validated with the remaining portion of the total data.

Table 5.5: Goodness of Fit metrics for linear models trained with data points below a power threshold and validated with data points above a power threshold P

Fit Name	R^2	DFE	RMSE (μm)	V RMSE (μm)
P<= 6.5	0.02	18	194	215
P<= 7.5	0.18	29	193	197
P<= 8.5	0.37	40	193	267

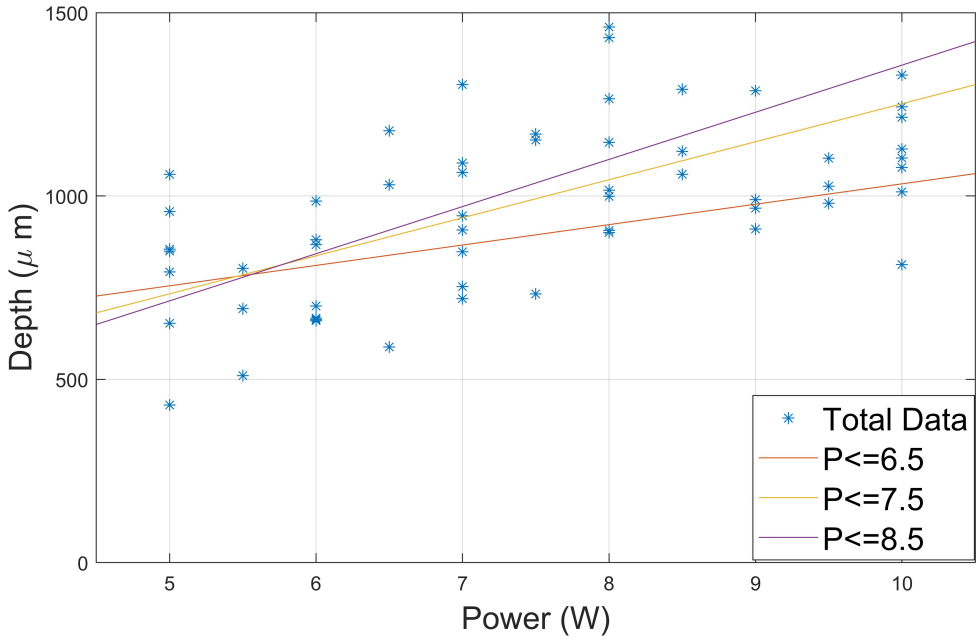

Figure 5.9: Linear Models trained using varying power levels from total data and validated against higher power levels

Fig. 5.10 and Table 5.6 show the results of logarithmic models trained using varying power levels and validated with the remaining data using the total data.

Table 5.6: Goodness of Fit metrics for logarithmic models trained with data points below a power threshold and validated with data points above a power threshold P

Fit Name	R^2	DFE	RMSE (μm)	V RMSE (μm)
P<= 6.5	0.02	18	195	239
P<= 7.5	0.18	29	195	180
P<= 8.5	0.37	40	196	211

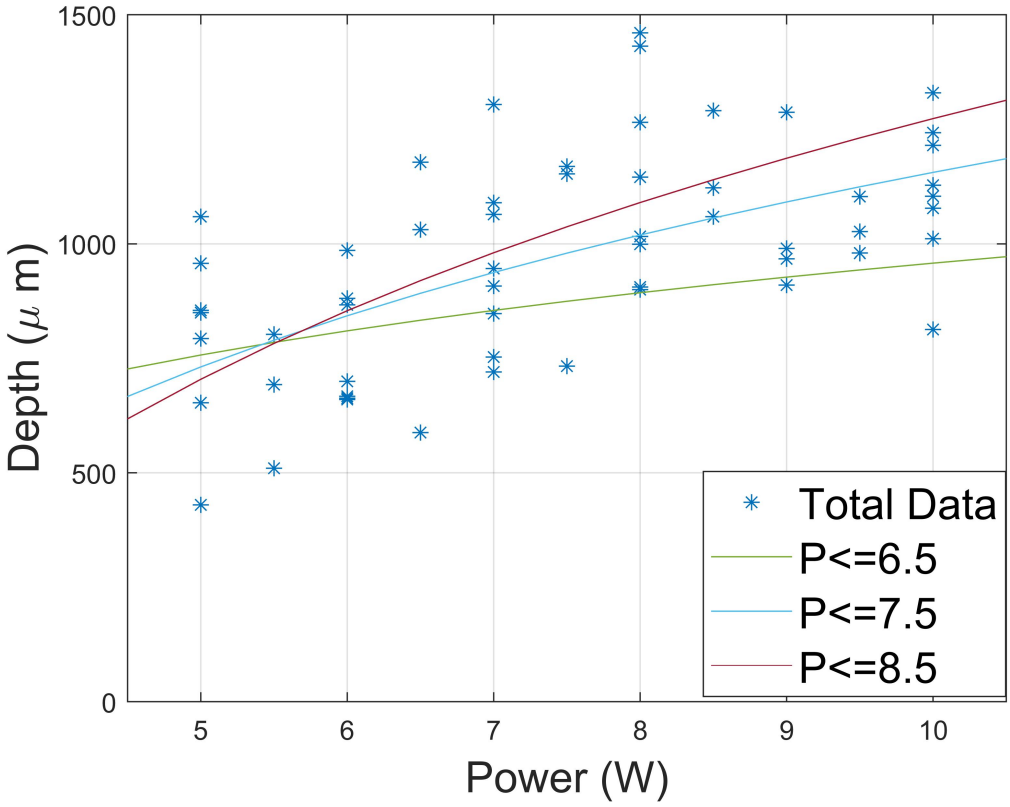

Figure 5.10: Logarithmic Models trained using varying power levels from total data and validated against higher power levels

A paired t.test was performed to see if there was a difference between linear and logarithmic fit validation RMSE values using total data. The T.test failed, showing there was not significant difference.

Fig. 5.11 and Table 5.7 show the results of linear models trained using varying power levels and validated with the remaining data using the Temperature filtered data.

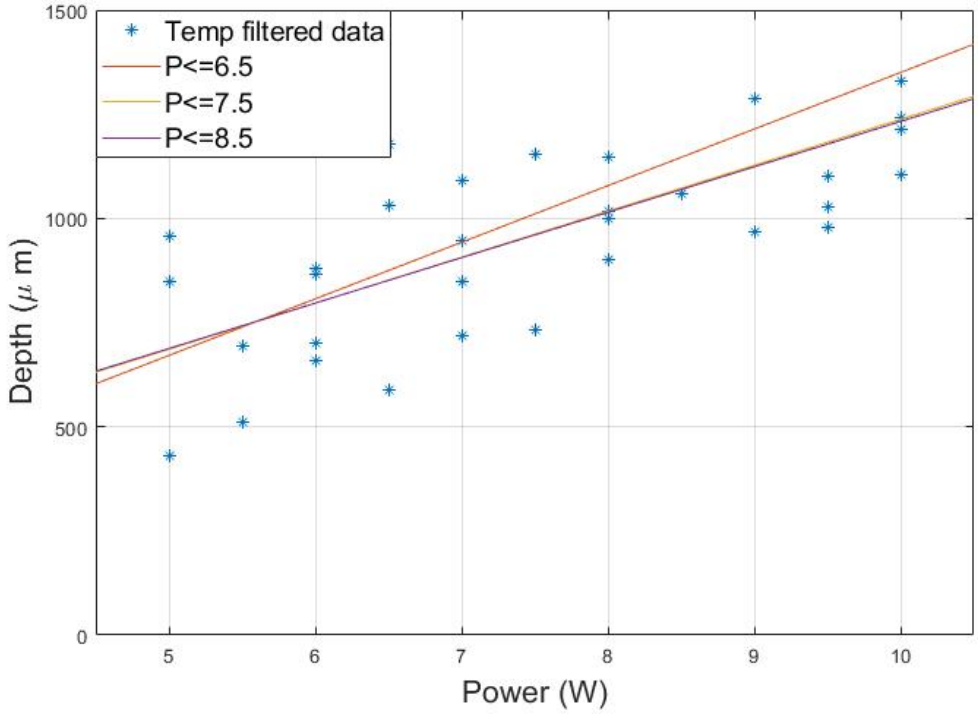

Figure 5.11: Linear Models trained using varying power levels from Temperature filtered data and validated against higher power levels

Table 5.7: Goodness of Fit metrics for linear models trained with temperature filtered data points below a power threshold and validated with data points above a power threshold P

Fit Name	R^2	DFE	RMSE (μm)	V RMSE (μm)
P<= 6.5	0.02	10	194	170
P<= 7.5	0.18	16	193	113
P<= 8.5	0.37	21	193	127

Fig. 5.12 and Table 5.8 show the results of logarithmic models trained using varying power levels and validated with the remaining data using the Temperature filtered data.

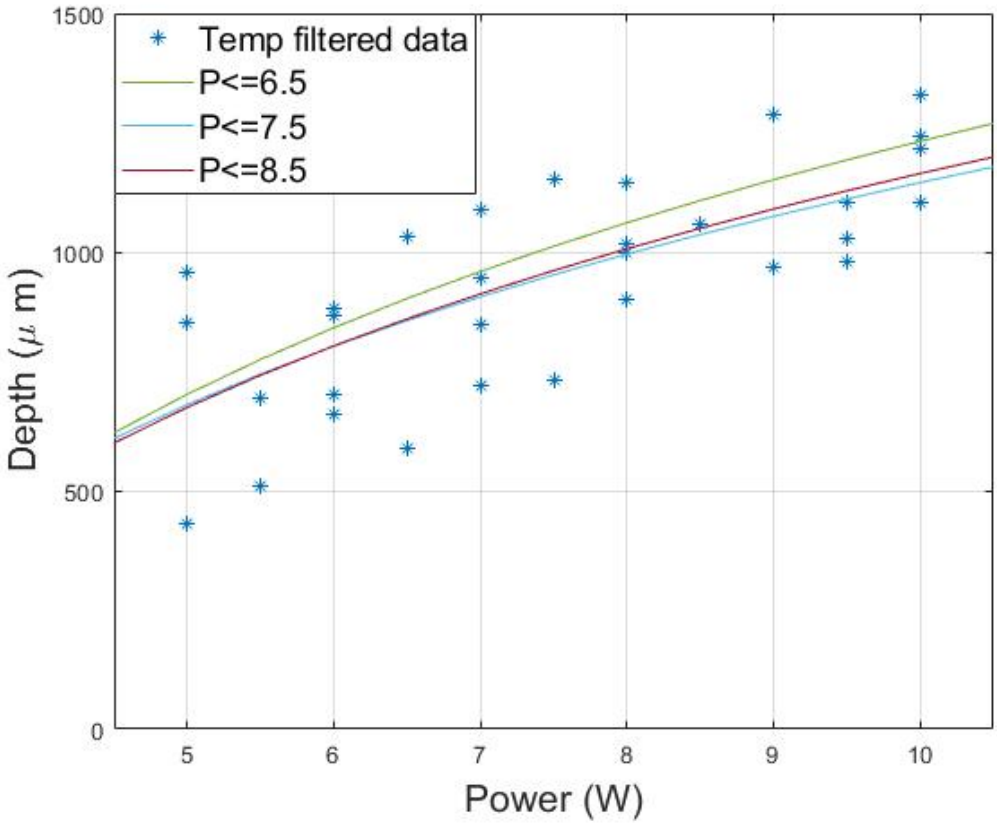

Figure 5.12: Logarithmic Models trained using varying power levels from Temperature filtered data and validated against higher power levels

A paired T.test was performed to see if there was a difference between linear and logarithmic fit V RMSE values using temperature filtered data. The t.test failed, showing there was not significant difference.

5.3.2 Discussion

In models created using the total data as seen in Tables 5.5 and 5.6, the V RMSE values for both the logarithmic and the linear fits were larger than the RMSE from models generated using the entire data, Fig. 5.4. While it does improve slightly, it never beats the RMSE of 163 μm seen in models created using temperature filtered

Table 5.8: Goodness of Fit metrics for logarithmic models trained with temperature filtered data points below a power threshold and validated with data points above a power threshold P

Fit Name	R^2	DFE	RMSE (μm)	V RMSE (μm)
P<= 6.5	0.12	10	217	127
P<= 7.5	0.18	16	199	108
P<= 8.5	0.30	21	178	118

data, seen in Fig. 5.7. The temperature filtered data performed far better for both linear and logarithmic fits. In the linear fit, Table 5.3, the V RMSE improved significantly and seemed to converge with P<= 7.5. In the logarithmic fit, Table 5.4 the V RMSE still improved but only slightly, and seemed to converge with P<= 7.5 as well. Overall, the logarithmic fit using Temperature filtered data performed the best but only incrementally. The t.test revealed that there was no significant difference between the goodness of fit metrics for linear or the logarithmic models trained with either total data or temperature filtered data.

5.4 Overall Discussion

It appears that both the linear equations and the logarithmic equations proposed can build accurate models up to 108 μm using metrics that can easily collected from an operating room, even when treating the laser system and the tissue target as black box components. Temperature filtered data enabled far better models compared to the total data models. One can argue that the temperature filtered data (temperature of 21 C +/- 1) has higher relevance clinically due to the body's ability to regulate and maintain a small range of temperature throughout the body. The test setup described in sections 4.2.2 and 4.2.3 was designed to keep the tissue moisturized and bring it up to temperature before laser action. The large temperature distribution was not intended and may have been a consequence of using a

fume extractor, which is also used in laser surgical procedures as well [1, 9]. It is unclear at this time how much temperature variance a fume extractor introduces on the tissue targets, or if they are activated only during tissue action or left on the whole time. While both linear and logarithmic models performed well, both in the randomized data points training and validation and in the Power threshold training and validation, and have similar predictions and V RMSE values, both diverge when looking at power levels lower than the training data. Notice how in all the logarithmic models, it predicts that a laser pulse with Power = 2 W emitted using our procedure would have a laser pulse depth of 0 micrometers. It also predicts a negative value for all Power values less than 2 W. This is untrue, as preliminary data shows that ablation did occur at these power levels and there was a noticeable depth, although difficult to measure.

As such, both the linear models and logarithmic models built on the fly could be used to predict the laser pulse depth for Power levels higher than the samples used to train the models, but it is hypothesized that the linear model might be able to predict for power levels higher and lower than the samples used to train the model better than the logarithmic model. However, the logarithmic model seems to excel in predicting data using lower power levels, as seen in table 5.8, when compared to the linear models in table 5.7. With better imaging and topography scanning equipment, such as a profilometer, one would be able to obtain accurate measurements for the ablations created with smaller powered laser pulses. Future studies are recommended where more accurate measuring systems that can be introduced in the operating room or similar to ones currently used in operating rooms. While temperature may not be much varied during the initial laser pulse, the temperature of the tissue around the ablation zone will have increased in temperature. This can make laser cutting using multiple pulses difficult to perform without also measuring

and accounting for temperature.

Chapter 6

Conclusions

Based on the experimental results, we can conclude that the proposed method of building accurate models on the fly using only information provided by the laser system and controlling for other parameters is feasible. Moreover, it is possible to acquire accurate approximations of higher power laser ablation depth using a range of data built using lower power. We can conclude that this method, proposed in hypothesis 2, is better than the randomization protocol most used in building predictive models, ie. randomly selecting laser parameters and recording the data. One thing of note is that temperature of the tissue target has a larger effect on laser pulse depth than previously assumed. While this may not affect predictions for initial pulses for a procedure (ie. the initial laser incision), I hypothesize that it would increase the maximum ablation depth of subsequent pulses in close proximity. We can conclude that temperature of the target has a measurable affect on the maximum ablation depth and should be monitored in all soft tissue laser surgical procedures.

The study encountered a number of limitations, the most important of which was the ability to collect data reliably only in the 5-10 W range. Another limitation

was our inability to quickly obtain the ablation profile for a single laser pulse. This increased the cost of data acquisition, and limited us to only using inactive samples (ie. already dead tissue). Live tissue is very active and would possibly inflame after being laser cut, possibly changing the ablation profile before measurements could be extracted using our methods. If this study is to be repeated on live specimen, it is recommended that an automated measurement process be explored.

For the future, it is recommended that both a feedback system incorporating a topography imager and a surgeon dependant optimization algorithm is investigated and the thought process of laser surgeons during the initial phases of the procedures are understood. It is also recommended to see how well these models perform when trying to predict a multiple pulse laser cut and to see how well interrogation pulses as little as 2 Watts can be used to predict the depth of a laser incision as high as 10 Watts.

Appendix A

Lab Equipment

This Appendix shows information regarding the following critical components of the experimental equipment:

- Franka Panda Robot
- FLIR A655sc Thermal Camera
- Leica CM 3050S Cryotome

A.1 CAD Models & Drawings

ITEM NO.	PART NUMBER	QTY.
1	BA_J1_adapted	1
2	SH_J1J2_adapted	1
3	SH_J2J3_adapted	1
4	EL_J3J4_adapted	1
5	EL_J4J5_adapted	1
6	LA_J5J6_adapted	1
7	WR_J6_adapted	1
8	WR_J7_adapted	1
9	CLAMPING_PROTECTOR_ELBOW_adapted	2
10	CLAMPING_PROTECTOR_ELBOW_SMALL_adapted	2
11	ELBOW_PROTECTOR_adapted	2
12	LOWER_ARM_PROTECTOR_adapted	1

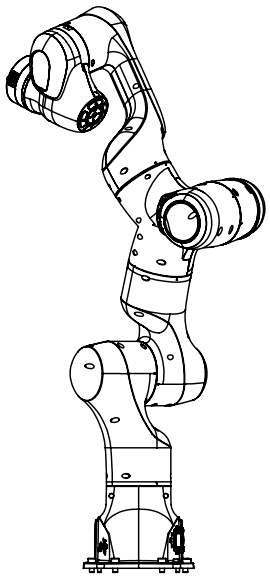

		UNLESS OTHERWISE SPECIFIED:		NAME	DATE
		DIMENSIONS ARE IN INCHES TOLERANCES: FRACTIONAL ± ANGULAR: MACH ± BEND ± TWO PLACE DECIMAL ± THREE PLACE DECIMAL ±	DRAWN		
			CHECKED		
			ENG APPR.		
			MFG APPR.		
		INTERPRET GEOMETRIC TOLERANCING PER:	Q.A.		
		MATERIAL	COMMENTS:		
NEXT ASSY	USED ON	FINISH			
APPLICATION		DO NOT SCALE DRAWING			

TITLE: Franka Panda Arm

SIZE	DWG. NO.	REV
A	FRANKA_movable	1

SCALE1:10	WEIGHT:	SHEET 1 OF 1

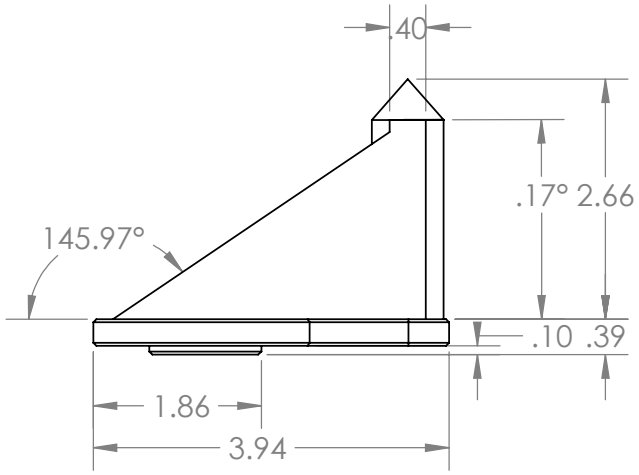

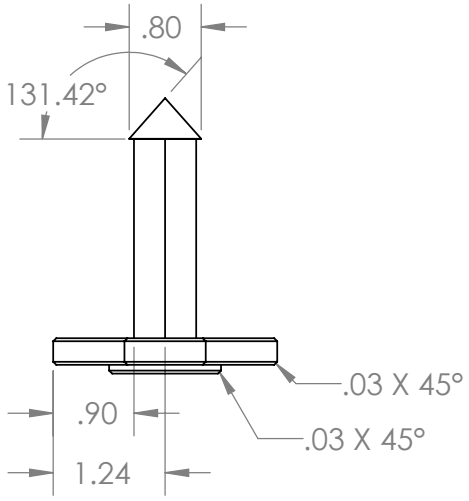

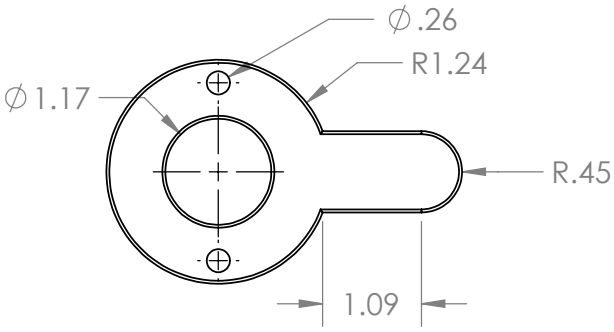

UNLESS OTHERWISE SPECIFIED: DIMENSIONS ARE IN INCHES SURFACE FINISH: TOLERANCES: LINEAR: ANGULAR:	FINISH: FDM 3D printed, no finish	DEBURR AND BREAK SHARP EDGES	DO NOT SCALE DRAWING / REVISION 1

	NAME	SIGNATURE	DATE
DRAWN			
CHK'D			
APPV'D			
MFG			
Q.A			

TITLE: Laser Waveguide Gripper

MATERIAL: PLA White	DWG NO. laser end effector_simplified	A4
WEIGHT:	SCALE:1:2	SHEET 1 OF 1

A.2 Specifications

FRANKA EMIKA

PANDA - DATASHEET [1]

May 2019

HARDWARE

Arm

Degrees of freedom	7
Payload	3 kg
Workspace	see backside
Maximum reach	855 mm
F/T Sensing	link-side torque sensors in all 7 axes
Expected nominal lifetime [3,4]	20,000 h
Joint position limits [°]	A1, A3, A5, A7: -166/166 A2: -101/101 A4: -176/-4 A6: -1/215
Mounting flange	DIN ISO 9409-1-A50
Installation position	upright
Weight	~ 17.8 kg
Moving mass	~ 12.8 kg
Protection rating	IP30
Ambient temperature [2]	15 – 25 °C (typical) 5 – 45 °C (extended)
Air humidity	20 – 80 % non-condensing
Power consumption	• max. ~ 350 W • typical application ~ 60 W
Interfaces	• ethernet (TCP/IP) for visual intuitive programming with Desk • input for external enabling device • input for external activation device or safeguard • Control connector • Connector for end-of-arm tooling

Control

Controller size (19")	355 x 483 x 89 mm (D x W x H)
Supply voltage	100 – 240 V_{AC}
Mains frequency	47 – 63 Hz
Power consumption	~ 80 W
Active power factor correction (PFC)	yes
Weight	~ 7 kg
Protection rating	IP20
Ambient temperature	15 – 25 °C (typical) 5 – 45 °C (extended)
Air humidity	20 – 80 % non-condensing
Interfaces	• ethernet (TCP/IP) for internet and/or shop-floor connection • power connector IEC 60320-C14 (V-Lock) • Arm connector

SOFT-ROBOT PERFORMANCE

Motion

Joint velocity limits [°/s]	A1, A2, A3, A4: 150 A5, A6, A7: 180
Cartesian velocity limits	up to 2 m/s end effector speed
Pose repeatabillity	<+/- 0.1 mm (ISO 9283)
Path deviation [3]	<+/- 1.25 mm

Force

Sensing [3]

Force resolution	<0.05 N
Relative force accuracy	0.8 N
Force repeatability	<0.15 N
Force noise (RMS)	<0.035 N
Torque resolution	<0.02 Nm
Relative torque accuracy	0.15 Nm
Torque repeatability	<0.05 Nm
Torque noise (RMS)	<0.005 Nm

1 kHz Control [3]

Minimum controllable force (Fz)		0.05 N
Force controller bandwidth (-3 dB)		10 Hz
Force range [N]	Nominal case	Best case
Fx	-125 – 95	-150 – 115
Fy	-100 – 100	-275 – 275
Fz	-50 – 150	-115 – 155
Torque range [Nm]	Nominal case	Best case
Mx	-10 – 10	-70 – 70
My	-10 – 10	-16 – 12
Mz	-10 – 10	-12 – 12

Interaction

Guiding force	~ 2 N
Collision detection time	<2 ms
Nominal collision reaction time [3,4]	<50 ms
Worst case collision reaction time [3]	<100 ms
Adjustable translational stiffness	0 – 3000 N/m
Adjustable rotational stiffness	0 – 300 Nm/rad
Monitored signals	Joint position, velocity, torque Cartesian position, velocity, force

ADD-ONS

Safety retrofit option with safety-rated PLC	PLd Cat. 3 • Safe torque off (STO) • Safe OSSD inputs
Fully integrated end effectors	• 2-finger gripper • Vacuum gripper
Fast mounting	Paw
Demonstration	Pop-up Box
Research interface	1kHz Franka Control Interface
Fieldbuses	Modbus/TCP, OPC UA, Profinet

LWIR SCIENCE-GRADE CAMERA

FLIR A655sc™

With its uncooled, high-resolution detector and cutting-edge functionality, the FLIR A655sc helps researchers and scientists accurately quantify thermal patterns, leakage, dissipation, and other heat related factors in equipment, products, and processes in real-time.

www.flir.com/science

SUPERIOR IMAGE QUALITY & SENSITIVITY

Record crisp thermal images, even at high speeds

- Produce clearly detailed 640 x 480 thermal images using the maintenance free vanadium oxide (VoX) microbolometer
- Detect temperature differences as small as 50 mK
- Record 14-bit, full-frame data at up to 50 Hz, or 200 Hz with windowing

EASY, FLEXIBLE DATA COLLECTION

True plug and play connectivity simplifies data monitoring and sharing

- Fast image transfer over GigE Vision, using low-cost standard cables up to 100 meters
- Integrate with FLIR ResearchIR or third-party software seamlessly over Gigabit Ethernet connections
- Control the camera with GenICam protocol support

ADVANCED SOFTWARE COMPATIBILITY

Get more out of your data with advanced analysis tools

- Control and capture data directly intoFLIR ResearchIR Max or MathWorks® MATLAB
- Stream data directly to a PC running software for live viewing, recording, analysis, and sharing.
- Integrate with your proprietary software through optional Software Developers Kit (SDK)

Motorcycle break testing.

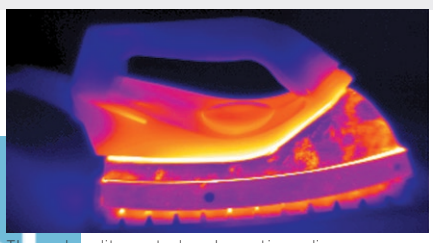

Thermal quality control on domestic appliances.

IMAGING SPECIFICATIONS

System Overview	FLIR A655sc
Detector Type	Uncooled Microbolometer
Spectral Range	7.5 – 14.0 µm
Resolution	640 x 480
Detector Pitch	17 µm
NETD	<30 mK
Imaging	
Time Constant	<8 ms
Frame Rate (Full Window)	50 Hz
Subwindow mode	User-Selected, 640 x 240 or 640 x 120 (Gigabit Ethernet Only)
Maximum Frame Rate (@ Min. Window)	200 Hz (640 × 120)
Dynamic Range	16-bit
Digital Data Streaming	Gigabit Ethernet (50/100/200 Hz) USB(25 Hz)
Command and Control	Gigabit Ethernet, USB
Measurement	
Standard Temperature Range	–40°C to 150°C (–40°F to 302°F) 100°C to 650°C (212°F to 1,202°F)
Optional Temperature Range	Up to 2,000°C (3,632°F)
Accuracy	±2°C or ±2% of Reading
Optics	
Camera f/#	f/1.0
Available Lenses	6.5 mm (80°), 13.1 mm (45°), 24.6 mm (25°), 41.3 mm (15°), 88.9 mm (7°)
Focus	Automatic or Manual (Motorized)
Close-up / Microscopes	Close-up 25 µm, 50 µm, 100 µm
Image Presentation	
Digital Data	Via PC Using ResearchIR Software

General	
Operating Temperature Range	-15°C to 50°C (572°F to 3,632°F)
Storage Temperature Range	-40°C to 70°C (-40°F to 158°F)
Encapsulation	IP 30 (IEC 60529)
Bump / Vibration	25 g (IEC 60068-2-29) / 2 g (IEC 60068-2-6)
Power	12/24 VDC, 24 W Absolute Max.
Weight	0.9 kg (1.98 lb)
Size	216 × 73 × 75 mm (8.5 × 2.9 × 3.0 in)
Mounting	¼"-20 (on three sides), 2 x M4 (on three sides)

CORPORATE HEADQUARTERS
FLIR Systems, Inc.
27700 SW Parkway Ave.
Wilsonville, OR 97070
PH: +1 877.773.3547

SANTA BARBARA
FLIR Systems, Inc.
6769 Hollister Ave.
Goleta, CA 93117
PH: +1 805.690.6600

CANADA
FLIR Systems, Ltd.
920 Sheldon Court
Burlington, ON L7L 5K6
Canada
PH: +1 800.613.0507

LATIN AMERICA
FLIR Systems Brasil
Av. Antonio Bardella,
320 Sorocaba, SP 18085-852
Brasil
PH: +55 15 3238 7080

CHINA
FLIR Systems Co., Ltd
Rm 1613-16, Tower II
Grand Central Plaza
138 Shatin Rural Committee Rd.
Shatin, New Territories
Hong Kong
PH: +852 2792 8955955

EUROPE
FLIR Systems, Inc.
Luxemburgstraat 2
2321 Meer
Belgium
PH: +32 (0) 3665 5100

www.flir.com
NASDAQ: FLIR

17-1683-INS-A655sc Datasheet

FLIR® | The World's Sixth Sense®

Leica CM3050 S Research Cryostat

Primarily designed for the demanding needs of cryosectioning in biomedical, neuro-anatomical and pharmaceutical research

The Leica CM3050 S cryostat features superior user comfort with excellent safety standards for practically all types of cryosectioning applications.

It is the instrument of choice for all research applications and for advanced clinical cryosectioning needs.

Particularly when working with delicate specimens – for example brain samples in neuroscience – the precise specimen orientation and the specimen feed system guarantees reproducible, thin, serial sections of maximum quality.

Select a configuration

Configuration 1 (14903050S01) ▾

VIEW CONFIGURATIONS

CONTACT US for a quote.

Quote Request
+1 844 534 2262

Customer Support
+1 844 534 2262

SPECS

Technical Specifications

GENERAL

Width (with handwheel):	835 mm
Depth (cabinet only):	850 mm
Height:	1215 mm
Working height (armrest):	1025 mm
Weight (w/ motor and suct.):	193 kg
Operating temperature range:	18°C to 35°C
Maximum specimen size:	50 x 80 mm
Cutting speed:	Slow: 0-50 strokes/min, Fast: 0-85 strokes/min, Vmax: 85-90 strokes/min
Section thickness setting	0.5 to 300 µm
Maximum specimen size	40 mm x 55 mm
Horizontal specimen feed	25 mm
Vertical specimen stroke	59 mm
Specimen retraction	50 pm
Specimen precision orientation	by 8° (x/y/z axis)
Trimming	5 to 150 µm ± 0,5 µm in steps of 5, 10, 30, 50, 100 and 150 µm
Motorized coarse feed at two speeds	500 µm/s and 1,000 µm/s

Cutting speed ranges	0.1 mm/s to 170 mm/s, 0.1 mm/s to 100 mm/s, Vmax 210 mm/s
Temperature setting range	0°C to -40°C
Defrosting	programmable 1 automatic defrost cycle/24 h duration; from 6 to 12 min; manual defrosting
Freezing shelf temperature	Approx. -43°C at an ambient temperature of 22°C
Temperature setting range	-10°C to -50°C (+/-3 K)
Dimensions (W x H x D)	882 x 1040 x 766 mm
Weight (including microtome)	Approx. 180 kg
Power draw	1800 VA

Appendix B

Other Methods Explored

Different methods were explored in regards to experimental goal, test-sample selection, and data-acquisition.

B.1 Experimental goal

The early conception of the experiment proposed involved taking the measurements of laser cuts composed of multiple laser pulses. Initially, it was believed that a mostly uniform laser cut could be created out of multiple pulses using the velocity parameters suggested. But the images from the OCT test images revealed in a great amount of detail that the cuts created with multiple pulses are extremely uneven and spaced apart. It was due to this information that the focus on the experiment shifted from a laser cut created from multiple pulses to a single pulse ablation profile.

B.2 Samples

Before the arrival of the new robot, different kinds of samples were explored by manually laser cutting using different parameters, slicing, and making note on the

quality of the image. To ensure the sample was still viable, the measurements taken using microscopy were compared to previous data with the laser from Sam Moriartys summer research work. 2.5 percent agar phantoms, 2.5 percent agar phantoms with flour added for opacity, 3.5 percent agar and 5.5 percent gelatin phantoms, store bought shitake mushrooms, and parsley. All samples were laser cut, sliced, and imaged using the same microscope.

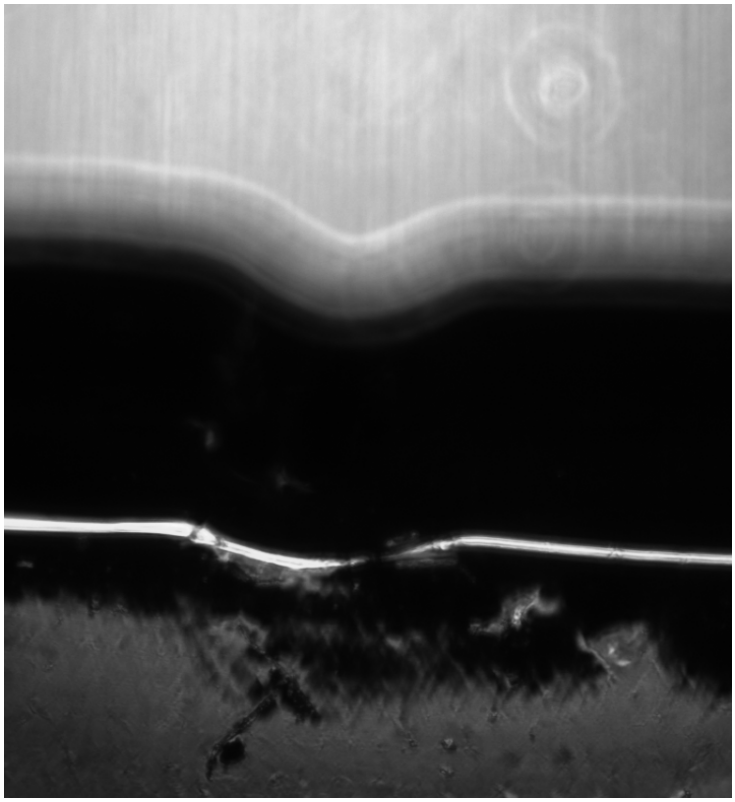

Figure B.1: cross sectional image of laser cut in 2.5 percent agar

2.5 percent agar phantoms [18], with and without flour for opacity, has been used in preliminary work for this project and has substantial data associated with robotic laser cutting with different settings that can be used to feed the algorithm. These models were originally used to create a low cost agar ultrasound phantoms. The problem encountered in recreating Sams test setup was the difficulty in slicing

and imaging. The 2.5 percent agar gel had a higher chance of plastically deforming during slicing, introducing error in the slicing and imaging process. The flour agar sample appeared to be comparably more plastic when palpated. Slicing and imaging lead to similar amounts of difficulty. Freezing samples lead them to shrivel and change volume.

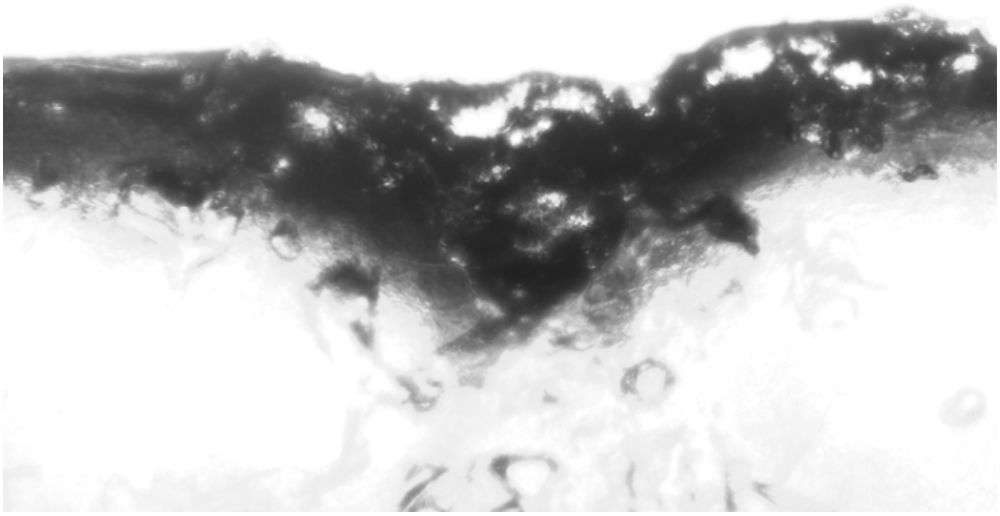

Figure B.2: Cross sectional image of 3.5 percent, 5 percent agar-gelatin phantoms

3.5 percent and 5.5 percent agar-gelatin phantoms, originally developed for Tissue-mimicking agar/gelatin materials for use in heterogeneous elastography phantoms, had considerably more elasticity, but were as easy to pierce or shear [19]. Surface did not appear to deform during cutting, but walls of the slice seemed to fragment and flake which introduced some noise in the image. The other issue encountered by this phantom and gel phantoms in general is the change in charac-

teristics of surface defects (such as cuts) when subjected to refrigeration, freezing, or open air over a couple hours.

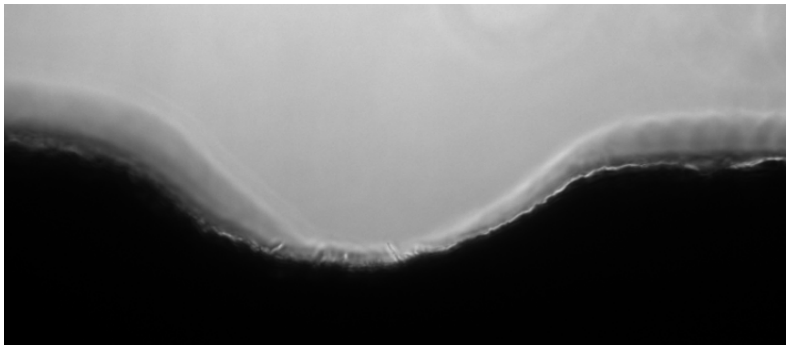

Figure B.3: Cross sectional image of Mushroom

Figure B.4: Image of mushroom showing different types of laser cut

Shitake mushroom slices were bought from the store and freshly laser cut. The laser cuts already appeared cleaner and more defined upon initial inspection, and the opacity of the mushroom made it a lot easier to identify the cut in a microscopic image. The mushroom slices had a good elasticity that allowed for easier cutting

and handling, and have a water composition similar to the 2.5 percent phantoms. While the mushroom samples appear better and seem to be easier to extract useful data on the shape of the cut, there didnt appear to be studies that use mushrooms as a testing model representative of any soft tissue.

Parsley used was also store bought. Initially, the idea was to simulate a more hydro dynamic test set up by cannulating and flowing warm saline through the parsley, similar to an artery. While this idea would certainly improve the hydrodynamics of the test set up, resecting a cancerous legion off of large vasculature that would not cauterize effectively would be a more specialized technique and outside the current scope for establishing the method. That being said, this set up can be revisited for testing the limits for this kind of method for really difficult laser resections.

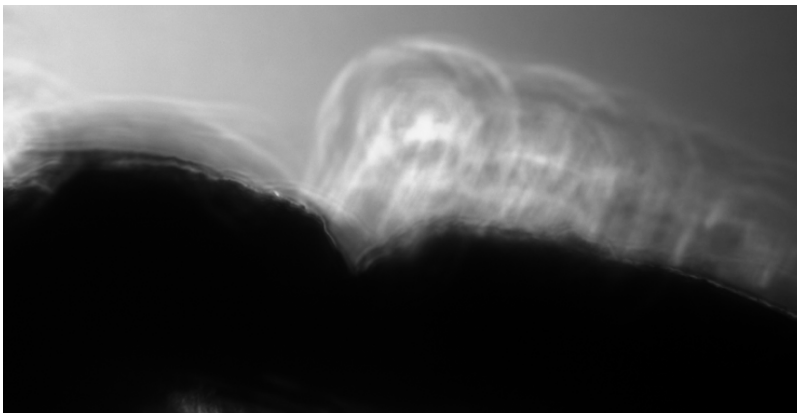

Figure B.5: cross sectional view of laser cut on the surface of parsley

B.3 Acquiring Depth measurements

A couple of methods were looked at for measuring depth accurately in-between or during laser cuts but were ruled out upon further research and preliminary tests/observation.

Early on at the recommendation of Dr. Zhang, Dr. Fichera and I got in touch with representatives at Santec, an OEM for OCT systems. OCT stands for Optical Coherence Tomography and has been used to provide high resolution optical images and measurements of various tissue and materials. Santecs specific product of interest was a minimally invasive approach to OCT scanning, particularly scanning with a laser fiber within vascular structures. We were fortunate enough to get some preliminary sample shipped to them and to have them image laser cuts that were done manually, see figure below, but ultimately our lab alone couldnt afford procuring their system and the time it would take to get a grant approved to acquire a system of our own would take longer than the remaining time for my thesis.

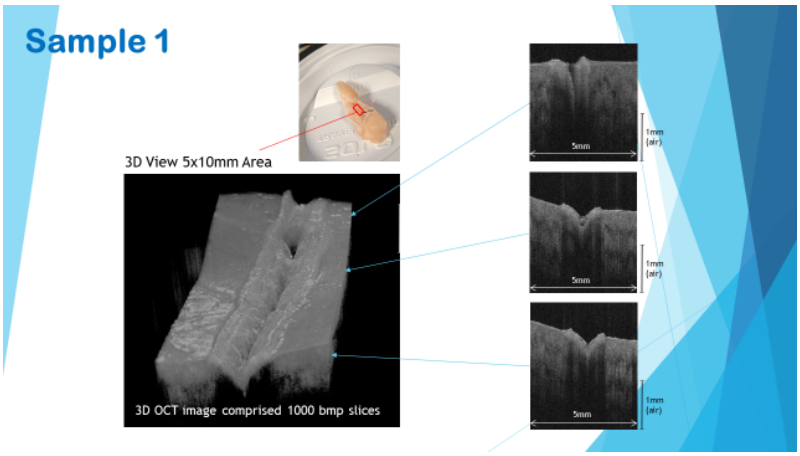

Figure B.6: (Top) OCT Images from continuous wave laser cut on chicken breast provided by Santec

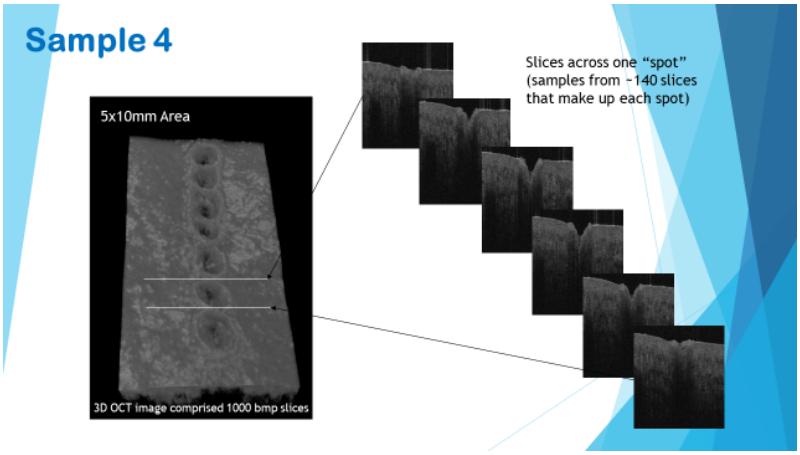

Figure B.7: OCT Images from Super Pulse laser cut on chicken breast provided by Santec.

B.4 Experimental Protocol

Initially, an additional fixture was used to keep the top of the tissue flat while allowing some exposure for the laser to interact with the tissue.

B.5 Modeling

Initially, when the experimental goal was centered on Laser cuts and not individual pulses, different methods for modeling the shape of the cut were explored. Originally Gaussian and quadranomial fits were explored to model the profile of a laser cut using a minimal amount of data points to avoid a rigorous sectioning process. When it became clear through the OCT images that these cuts were prone to unevenness due to a lack of understanding of individual laser pulse depth dimensions, it became clear that the focus was to shift towards modeling single pulses where a Gaussian fit made more sense.

Appendix C

Model building using separate data series

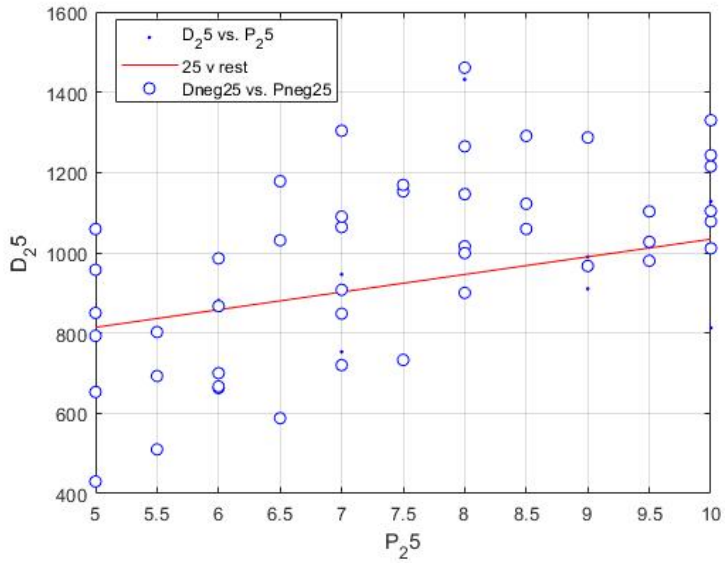

Figure C.1: Model Trained with Group 25, validated with the remaining 45 points

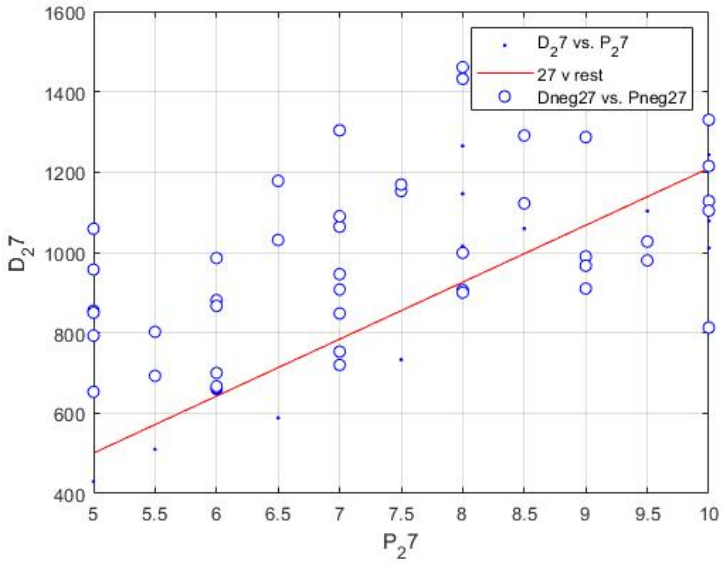

Figure C.2: Model Trained with Group 27, validated with the remaining 45 points

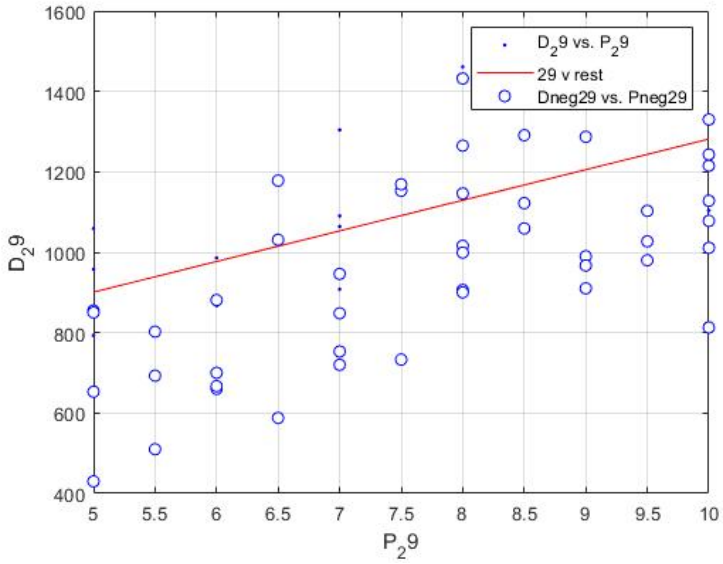

Figure C.3: Model Trained with Group 29, validated with the remaining 45 points

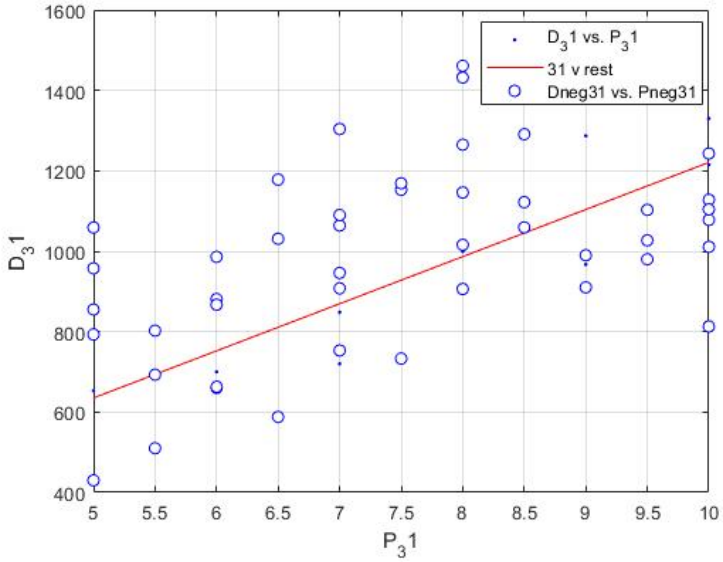

Figure C.4: Model Trained with Group 31, validated with the remaining 45 points

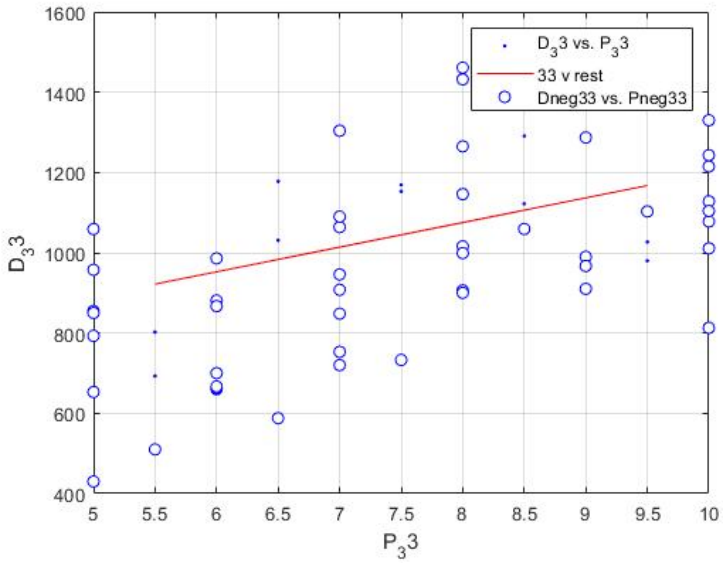

Figure C.5: Model Trained with Group 33, validated with the remaining 45 points

Below are the results of logarithmic models generated with a specific sample set (25,27,29,30,31,33) using this equation:

$$\hat{D} = b_1 * ln(P) + b_0 \tag{C.1}$$

and comparing the models generated with the rest of the data as validation data, where $\hat{D}$ is the estimated depth, P is the power level of the laser, b_1 and b_0 are coefficients.

Fit Name	SSE	Rsq	DFE	RMSE (μm)	V SSE	V RMSE (μm)
25 v Rest	3.629e5	0.14	9	202	1.88e6	200
27 v Rest	2.348e5	0.75	10	153	3.24e6	268
29 v Rest	3.703e5	0.27	10	192	2.36e6	228
31 v Rest	1.869e5	0.70	10	136	2.02e6	212
33 v Rest	2.038e5	0.31	8	159	2.03e6	207

Below are the results of linear models generated with a specific sample set (25,27,29,30,31,33) using this equation:

$$\hat{D} = b_1 * P + b_0 \tag{C.2}$$

and comparing the models generated with the rest of the data as validation data, where $\hat{D}$ is the estimated depth, P is the power level of the laser, b_1 and b_0 are coefficients.

Fit Name	SSE	Rsq	DFE	RMSE (μm)	V SSE	V RMSE (μm)
25 v Rest	3.627e5	0.13	9	202	1.92e6	204
27 v Rest	2.738e5	0.70	10	165	3.13e6	264
29 v Rest	3.778e5	0.26	10	194	2.41e6	231
31 v Rest	1.511e5	0.76	10	123	2.18e6	220
33 v Rest	2.234e5	0.25	8	167	2.10e6	211

Bibliography

[1] T. L. G. R. G. Hospital, *Atlas of CO2 Laser Surgical Techniques*. Laser surgical Technique series, St. Louis, MO and Tokyo: Ishiyaku EuroAmerica Inc., 1988.

[2] L. Fichera, *Cognitive supervision for robot-assisted minimally invasive laser surgery*. Springer theses, Switzerland: SpringerOpen, 2016.

[3] J. Hecht, *Understanding fiber optics*. Auburndale, Massachusetts: Laser Light Press, fifth edition, revised. ed., 2015.

[4] J. A. Harrington, *Infrared fibers and their applications*. PM135, Bellingham, Wash: SPIE Press, c2004.

[5] P. Patimisco, V. Spagnolo, M. S. Vitiello, G. Scamarcio, C. M. Bledt, and J. A. Harrington, "Low-loss hollow waveguide fibers for mid-infrared quantum cascade laser sensing applications," *Sensors (Basel)*, vol. 13, no. 1, pp. 1329–40, 2013.

[6] M. H. Niemz, *Laser-Tissue Interactions Fundamentals and Applications*. Biological and Medical Physics, Biomedical Engineering, Berlin, Heidelberg: Springer Berlin Heidelberg, third, enlarged edition. ed., 2007.

[7] . Alfred Vogel* and V. Venugopalan, "Mechanisms of pulsed laser ablation of biological tissues," *Chemical Reviews*, vol. 103, no. 2, pp. 577–644, 2003.

[8] Sharplan, "Sharplan 30c co2 surgical laser system user's manual," 2000.

[9] C. A. Puliafito, *Laser Surgery and Medicine: principles and Practice.* John Wiley and Sons Inc., 1996.

[10] L. Fichera, D. Pardo, P. Illiano, J. Ortiz, D. G. Caldwell, and L. S. Mattos, "Online estimation of laser incision depth for transoral microsurgery: approach and preliminary evaluation," *International Journal of Medical Robotics and Computer Assisted Surgery*, vol. 12, no. 1, pp. 53,61, 2016-03.

[11] S. L. Jacques, "Optical properties of biological tissues: a review," *Physics in Medicine and Biology*, vol. 58, no. 11, pp. R37,R61, 2013-06-07.

[12] W. Shen, J. Zhang, and F. Yang, "Modeling and numerical simulation of bio-heat transfer and biomechanics in soft tissue," *Mathematical and Computer Modelling*, vol. 41, no. 11, pp. 1251,1265, 2005.

[13] J. Zhang, J. Duan, and L. Gong, "Super pulse co2 laser therapy for benign eyelid tumors," *Journal of Cosmetic Dermatology*, vol. 17, no. 2, pp. 171,175, 2018-04.

[14] C.-S. Lai, C.-T. Lu, S.-A. Liu, Y.-C. Tsai, Y.-W. Chen, and I.-C. Chen, "Robot-assisted microvascular anastomosis in head and neck free flap reconstruction: Preliminary experiences and results," *Microsurgery*, vol. 0, no. 0.

[15] K. Hashimura, K. Ishii, N. Akikusa, T. Edamura, H. Yoshida, and K. Awazu, "Coagulation and ablation of biological soft tissue by quantum cascade laser with peak wavelength of 5.7 m," *Journal of Innovative Optical Health Sciences*, vol. 7, no. 3, pp. 1450029–1–1450029–9, 2014-05.

[16] USDA, "Chicken from farm to table," 2014.

[17] M. John, "Pattern recognition and machine learning," *Journal of Statistical Software*, vol. 17, no. 1, pp. 1–3, 2007.

[18] M. Earle, G. D. Portu, and E. DeVos, "Agar ultrasound phantoms for low-cost training without refrigeration," *African Journal of Emergency Medicine*, vol. 6, no. 1, pp. 18–23, 2016.

[19] E. L. Madsen, M. A. Hobson, H. Shi, T. Varghese, and G. R. Frank, "Tissue-mimicking agar/gelatin materials for use in heterogeneous elastography phantoms," *Physics in medicine and biology*, vol. 50, no. 23, pp. 5597–5618, 2005.